博 士 論 文

Studies on structures and properties of nanocellulose/layered silicate composites

（ナノセルロース／層状ケイ酸塩複合体の構造と特性に関する研究）

WU Chun-Nan

Table of contents

Chapter 1
General introduction

1.1 Polymer/layered silicate nanocomposite

1.1.1 Characteristics

Natural organic/inorganic composites, such as seashell nacre, crustacean exoskeletons, and deer antlers, show excellent mechanical properties.[1] Nacre is representative of such natural composites and have recently been attracting much attention in the field of materials science. Nacre has a unique layered hierarchical structure that is composed of plate-like calcium carbonate and adhesive organic biopolymers.

A man-made material inspired by the nacre structure is polymer/layered silicate (PLS) nanocomposites. The PLS nanocomposites have been used in a range of practical materials from automobile parts to packaging materials. Layered silicate is derived from natural clay minerals, which is a material consisting of plate-like particles with thickness a few nanometers. When these silicate nanoplatelets, so-called nanoclay, are incorporated into polymer matrices as a filler, mechanical, thermal, and gas-barrier properties of the host polymeric materials are effectively improved as compared with other fillers.[2,3] The earliest example of PLS nanocomposite was shown by researchers at Toyota; they prepared a nanocomposite from nylon 6 and a layered silicate and found significant improvement in the mechanical and thermal properties.[4,5] Later, many other researchers embraced the new composite material concept and further developed many PLS combinations, composite nanostructures, and synthesis methods.

Silicate nanoplatelets have significant advantages compared with other fillers used in the polymer composite materials, such as glass fibers; silicate nanoplatelets have higher aspect ratios, or the ratios of the platelet size to the thickness, and can exhibit the reinforcement effects in all the directions parallel to the platelet surfaces. For example, it has been reported that the reinforcement efficiency of silicate nanoplatelets in Nylon 6 matrix is three times higher than that of glass fibers; nylon 6 composites reinforced by glass fibers have the same Young's moduli as those reinforced by silicate nanoplatelets with one third amount of the glass fibers.[6] It is also advantageous that clay minerals containing layered silicate are

abundant in nature and low in price.

1.1.2 Structure

The silicate nanoplatelets in natural clay minerals are stacked on top of each other and form bulky assemblies. These nanoplatelets are hydrophilic, and are combined with each other by van der Waals' force.[2] Therefore, separating each nanoplatelet, or dispersing the individual nanoplatelets into polar fluids including water is relatively easy. The dispersion of silicate nanoplatelets is important in the polymer reinforcement; the dispersed nanoplatelets have higher aspect ratios than their aggregates, resulting in the higher reinforcement efficiency. The dispersion of silicate nanoplatelets in the polymer matrix can be evaluated by X-ray diffraction analysis. On the basis of the nanoplatelets dispersion state within the polymer matrix, the PLS nanocomposites are categorized into three types: immiscible, intercalated, and exfoliated states (Figure 1.1).[3] The immiscible state denotes the composite structure that silicate nanoplatelets are not dispersed in the polymer matrix but distributed as their aggregates. In contrast, silicate nanoplatelets are completely dispersed as the indivudual platelets in the exfoliated state. The intercalated state is an intermidiate state between the immiscible and the exfoliated states, which assumes the state that polymer chains are intercalated to the minute spaces between the nanoplatelets, and the interplanar spaces are slightly expanded.

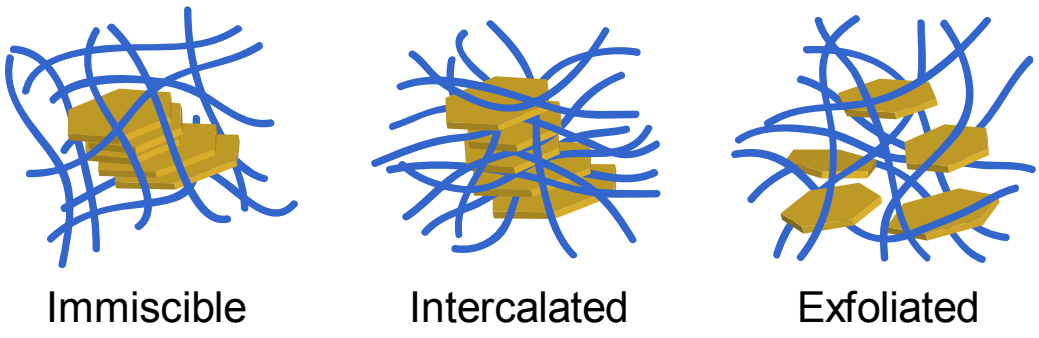

Figure 1.1. Three different separation types of silicate nanoplatelets in polymer matrix.

Silicate nanoplatelets are, however, hydrophilic. Thus, it is difficult to disperse such hydrophilic nanoparticles into hydrophobic polymer matrices. Silicate nanoplatelets are often modified using cationic surfactants with long alkyl chains to be organophilic to prepare PLS nanocomposites with hydrophobic polymers. It was reported that the surfactant-modified nanoplatelets, so-called organoclay, disperse well in hydrophobic polymer matrices, resulting in the improvement of material properties. These surfactants act to expand the galleries between the nanoplatelets, which allows the polymer chains to more easily intercalate between the nanoplatelet layers. Various types of polymers, such as polyolefins and polyamides, have been combined with these organoclays. In general, hydrophobic PLS nanocomposites are prepared by 1) cast-drying of the mixed dispersions of the organoclays and host polymer molecules, 2) in situ polymerization of the host polymers using the monomer solutions including organoclays, or 3) the melt extrusion of host polymer and organoclay.

1.2 Layered silicate

1.2.1 Classification

Silicates are the most abundant minerals on earth, which form over 90% of earth's crust and mantles. The structural unit of silicates is silicon tetraoxide, $(SiO_4)^{4-}$. These tetrahedral units are linked to one another in different manners, resulting in the formation of various conformations, such as rings, single chains, double chains, sheets, and frameworks (Figure 1.2). The layered silicates, which are used in PLS composites, are found in clay minerals and consist of the sheet-shaped silicates. These layered silicates are further categorized into the following five groups according to the higher-order structures and chemical compositions (Figure 1.3): smectite, illite, vermiculite, kaolinite, and chlorite.[7] Each layered silicate shows different properties and are widely used in various fields. In particular, the smectite-type silicates, which is a major component of swelling clay minerals, have attracted attention due to their high surface-charge amounts and large specific surface areas.[8]

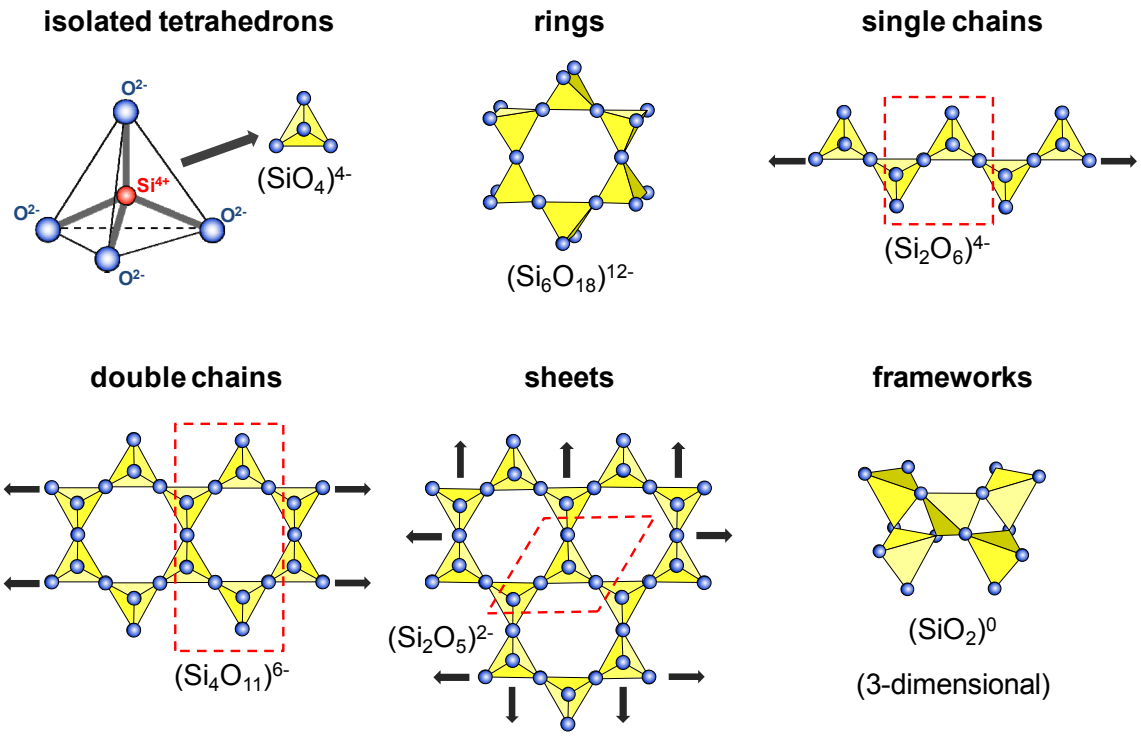

Figure 1.2. Linking patterns of the tetrahedral silicon tetraoxide units in minerals.

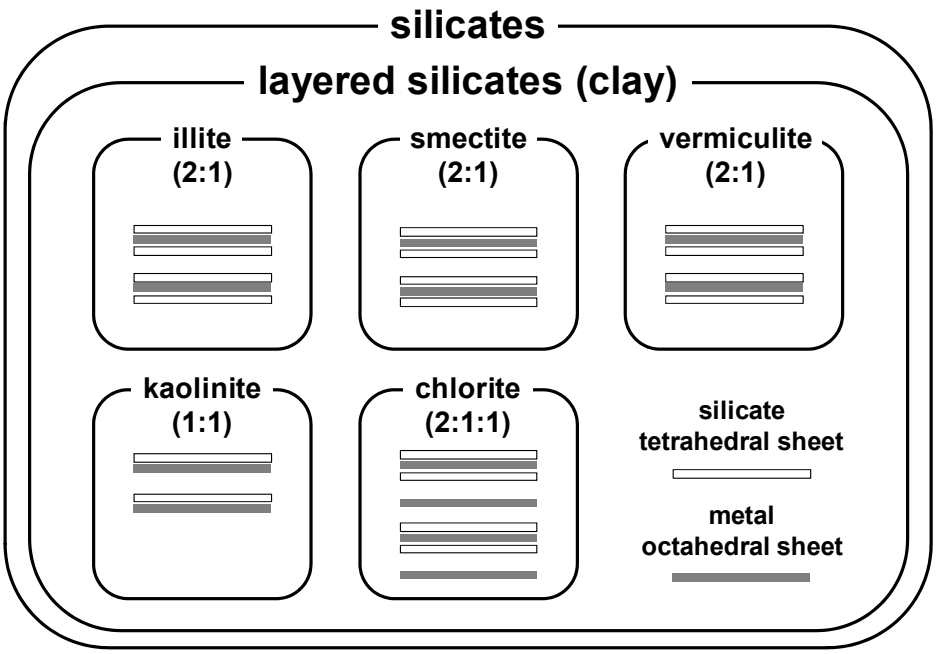

Figure 1.3. Structural classification of layered silicates in clay minerals.

1.2.2 Montmorillonite and saponite

Representative layered silicates used in industry are montmorillonite (MTM) and saponite (SPN), both of which belong to the smectite group. Figure 1.4 shows the hierarchical structures of MTM in clay-rich minerals. The MTM nanoplatelet is about 1 nm thick, and has a sandwiched structure comprising an inner octahedral metal layer and two outer silicate tetrahedral layers. In the outer silicate layers, some of central silicon ions, Si^{4+}, are substituted with other metal ions, Al^{3+} or Mg^{2+}, such that the surface of a MTM nanoplatelet is negatively charged.[3,9] In contrast, the edges of the MTM nanoplatelets are positively charged.[10,11] The MTM nanoplatelets are very similar in structure to SPN ones. The differences between MTM and SPN are that, 1) the silicon ions are substituted mainly with Al^{3+} and Mg^{2+}, respectively, and 2) the platelet size of SPN (~50 nm) is much smaller than that of MTM (~300 nm).[6,10]

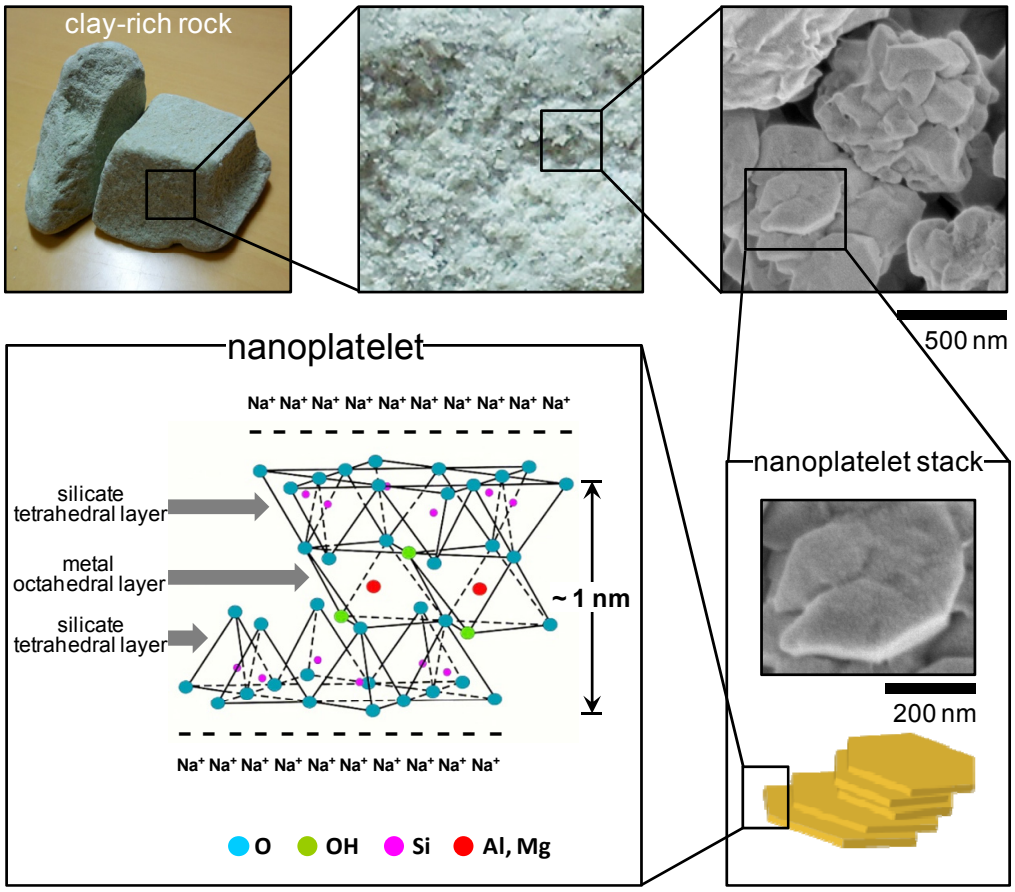

Figure 1.4. The hierarchical structures of MTM.

1.3 Nanocellulose

1.3.1 Cellulose

Cellulose is the most abundant polymer on earth and a major component of wood biomass, which is thus a key source of sustainable materials on an industrial scale.[12,13] For quite a long time, cellulose has been used in the form of wood and fibers as an energy source, building materials, clothing, and papers. Cellulose is a linear polysaccharide consisting of β-1,4-linked D-glucose units. The equatorial and axial directions of the glucopyranose are hydrophilic and hydrophobic, respectively (Figure 1.5), so that cellulose molecules have amphiphilic nature. Figure 1.6 shows the hierarchical structures of wood cellulose.[12] The cellulose microfibrils consist of fully extended and uniaxially aligned cellulose chains, and have uniform widths of ~3 nm, length of more than 1 μm, and high crystallinity. Owing to these structural characteristics, cellulose microfibrils and their assemblies exhibit high mechanical properties and high thermal stability.

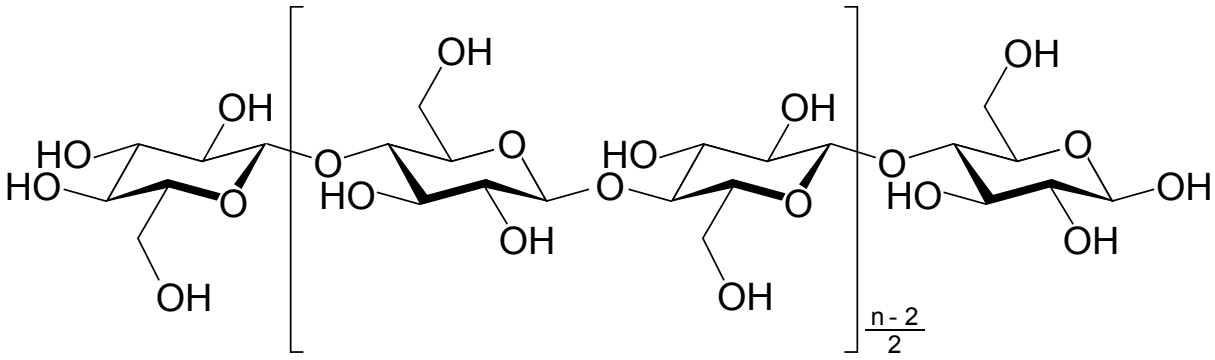

Figure 1.5. Molecular structure of cellulose. The n is the degree of polymerization.

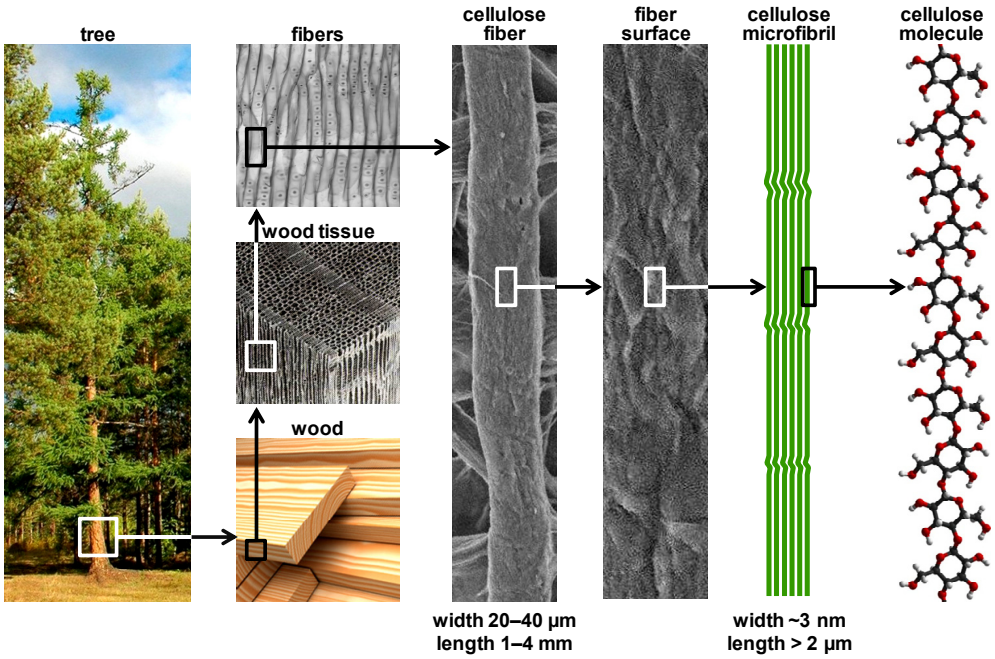

Figure 1.6. The hierarchical structures of wood cellulose.[12]

1.3.2 Nanocellulose

In recent years, cellulose microfibrils have been attracting much attention as a new biobased nanomaterial with excellent properties, so-called "nanocellulose". However, because individual cellulose microfibrils are firmly agglomerated with each other in wood cell walls, it is essential to fibrillate cellulose before new materials consisting of cellulose microfibrils can be formed. Hence, material scientists have devoted much effort for dispersing cellulose microfibrils.

Nanocelluloses are classified in three subcategories based on the sources and preparation methods: nanofibrillated cellulose (NFC), nanocrystalline cellulose (NCC), and bacterial nanocellulose (BNC) (Table 1.1).[13] In general, NFC-based materials show superior mechanical properties to those of NCC ones because of the higher aspect ratios of NFC. Besides, the yields of NFCs (~100%) are much higher than those of NCCs (< 50%).[12] NFCs are generally prepared from bleached wood pulp/water slurries through repeated high-pressure homogenizer treatments to partially cleave numerous linkages between cellulose microfibrils. However, these mechanical treatments require high energy input of

700–1400 MJ kg^{-1}. Still, the resulting fibrillated celluloses consist of thick bundles of cellulose microfibrils. In this context, it has been proved that chemical or enzymatic pretreatment of wood celluloses is a promising way to obtain thinner fibrils with small energy input.[12]

Table 1.1. Classification of nanocelluloses.[13]

Type	Synonyms	Sources	Preparation and average size
nanofibrillated cellulose (NFC)	microfibrillated cellulose microfibrils nanofibrils	wood, sugar beet, potato tuber, hemp, flax	delamination of wood pulp by mechanical pressure before and /or after chemical or enzymatic treatment diameter: 5–60 nm length: several micrometers
nanocrystalline cellulose (NCC)	cellulose nanocrystals crystallites whiskers rodlike cellulose microcrystals	wood, cotton, hemp, flax, wheat straw, mulberry bark, ramie, tunicin, cellulose from algae and bacteria	acid hydrolysis of cellulose from many sources diameter: 5–70 nm length: 100–250 nm (from plant celluloses); 100 nm to several micrometers (from celluloses of tunicates, algae, and bacteria)
bacterial cellulose (BNC)	bacterial cellulose microbial cellulose biocellulose	low-molecular-weight sugars and alcohols	bacteria synthesis diameter: 20–100 nm; different types of nanofiber networks

1.3.3 TEMPO-oxidized cellulose nanofibrils

Wood cellulose can be dispersed as completely individualized microfibrils through 2,2,6,6-tetramethylpiperidinyl-1-oxyl (TEMPO)-mediated oxidation and subsequent mild mechanical treatment in water.[14] TEMPO is a commercially available and stable nitroxyl radical. When TEMPO is used together with sodium bromide and sodium hypochlorite in water at room temperature under weakly alkaline condtions, primary hydroxyl groups of polysaccharides can be selectively oxidized to carboxyl ones. Primary hydroxyl groups of cellulose correspond to the C6 hydroxyl groups. Figure 1.7 shows the reaction mechanism for TEMPO-mediated oxidation of cellulose microfibrils under alkaline conditions.[15] In the TEMPO-mediated oxidation of cellulose, all the C6 hydroxyl groups exposed on the microfibril surfaces can be coverted to sodium carboxylate groups with preserving the crystalline structure of microfibril, or cellulose I strucuture. As a result, the oxidized microfibril surfaces have a regular chemical stucture; the oxidized surface molecules are

glucose/glucuronic acid alternatig copolymers. The sodium carboxylate groups on the microfibril surfaces are fully dissociated in water, so that repulsive forces, such as the electrostatic repulsion and/or osmotic pressure, work between the surface-carboxylated microfibrils in water. These surface-carboxylated microfibrils can be completely dispersed or isolated in water by mild mechanical disintegration treatment of small energy input (< 7 MJ kg^{-1}). The microfibrils thus dispersed in water are called TEMPO-oxidized cellulose nanofibrils (TOCNs), which is regarded as a NFC material with the narrowest fibril width and highest aspect ratios in the nanocellulose family.

TOCNs have a uniform width of ~3 nm and length of 0.3–2 μm. The TOCN length can be controlled by changing the preparation conditions such as reagent dose in TEMPO-mediation oxidation and mechanical treatment time. TOCNs have high mechanical strength, high elastic modulus, low coefficient of thermal expansion, and large specific surface area, originating from the nature of native cellulose microfibrils. Therefore, structured bulk materials of TOCNs, such as films and gels, exhibit excellent material properties. For example, TOCN films show high optical transparency, high mechanical strength, high thermal stability, and high oxygen barrier property.[16]

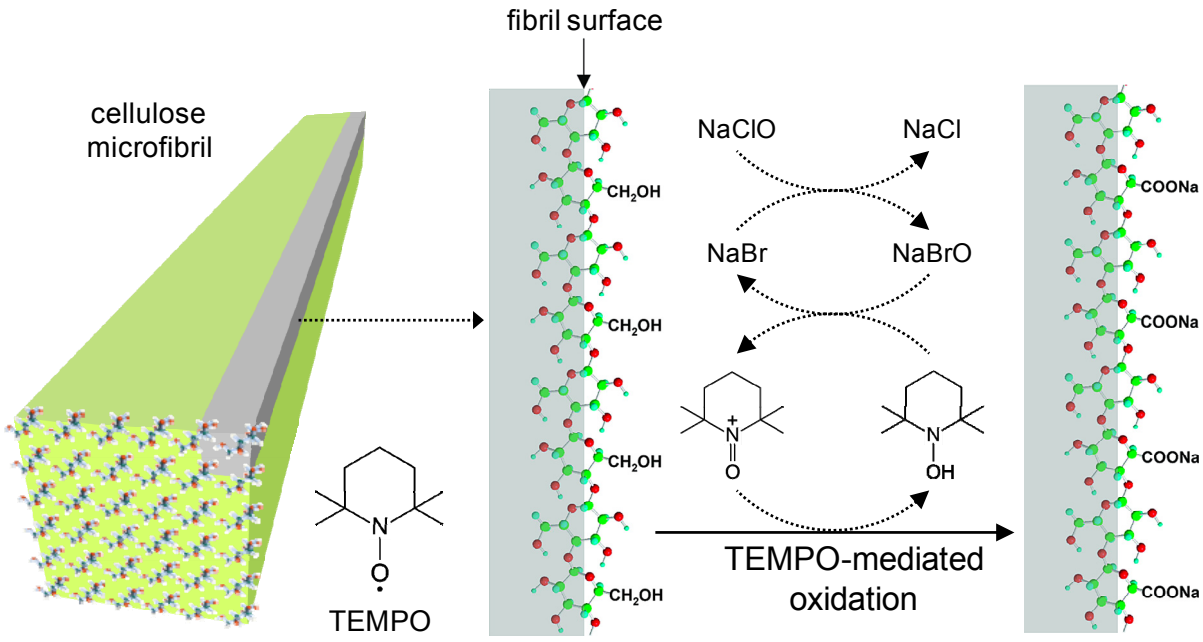

Figure 1.7. Oxidation of cellulose microfibrils by TEMPO/NaBr/NaClO system.[15]

1.4 Scope of the thesis

A new type of PLS nanocomposites is prepared from TOCNs and layered silicates through a simple process of cast-drying their water dispersions. These TOCN/layered silicate composites are assemblies of solid nanoparticles, which are inherently different in structure from previously reported PLS composites that can be categorized into the three structures shown in Figure 1.1. The TOCNs used as the polymer matrix component are thermally stable (no T_g, no T_m, and T_d ~300 °C), and the TOCN/layered silicate composites are thus similar in structure to natural nacres that are composed of calcium carbonate platelets and nanofibrillar chitin/protein hybrids rather than the conventional PLS composites of a man-made, nacre-inspired material. It should be added that the TOCN/layered silicate composites are a structurally new composite material that is composed of nanofibrillar polymer network and layered inorganic nanoparticles as a continuous matrix phase and reinforcing fillers, respectively. Thus, characterization of the TOCN/layered silicate composites are significant in the field of composites science. Furthermore, this study contributes to a development of the nanocellulose of a new biobased nanomaterial, which will disclose the potentials of nanocellulose for composites application.

In the present study, natural MTM and synthetic SPN nanoplatelets are used as the layered silicates. MTM nanoplatelets have higher aspect ratios than SPN ones, while SPN nanoplatelets have higher dispersibility in water than MTM ones. Both TOCNs and silicate nanoplatelets have abundant negative charges on their surfaces, so that repulsive forces such as electrostatic repulsion and/or osmotic pressure work between them in water, allowing the silicate nanoplatelets to be homogeneously distributed in the TOCN matrix.

This thesis is organized as follows:

In chapter 2, the TOCN/MTM composites are shown. The TOCN/MTM composites have distinct and closely-packed layered nanostructures, and exhibit extremely high mechanical strength comparable to those of steels and higher oxygen-barrier performances than commercial oxygen-barrier films.

In chapter 3, the TOCN/SPN composites are shown. The TOCN/SPN composites are highly transparent and show exceptionally high toughness. The high toughness of the TOCN/SPN composites is interpreted based on a model for fracture of polymer composites

reinforced with low-aspect-ratio platelets. Differences in mechanical and oxygen-barrier properties between the TOCN/MTM and the TOCN/SPN composites are explained based on those in aspect ratio between MTM and SPN nanoplatelets.

In chapter 4, water vapor permeabilities (WVP) and water contact angles (CA) of the TOCN/layered silicate composites are shown. The WVP of TOCN/layered silicate composites show a similar trend to their oxygen permeabilities. The CA increase with increasing silicate content, even though both TOCNs and silicate nanoplatelets are hydrophilic. This strange increase in CA is interpreted based on the surface microstructures of the composite films.

Chapter 5 is conclusive remarks.

1.5 References

(1) M. A. Meyers, J. McKittrick, and P.-Y. Chen, *Science*, **2013**, *339*, 773–779.

(2) S. S. Ray and M. Okamoto, *Prog. Polym. Sci.*, **2003**, *28*, 1539–1641.

(3) D. R. Paul and L. M. Robeson, *Polymer*, **2008**, *49*, 3187−3204.

(4) A. Usuki, Y. Kojima, M. Kawasumi, A. Okada, Y. Fukushima, T. Kurauchi, and O. Kamigaito, *J. Mater. Res.*, **1993**, *8*, 1179–1184.

(5) A. Okada and A. Usuki, *Mater. Sci. Eng. C*, **1995**, *3*, 109–115.

(6) T. D. Fornes and D. R. Paul, *Polymer*, **2003**, *44*, 4993–5013.

(7) G. Sposito, *The Chemistry of Soils*, Oxford University Press, New York, **1989**.

(8) H. H. Murray, *Appl. Clay Sci.*, **2000**, *17*, 207–221.

(9) J. Wang, Q. Cheng, and Z. Tang, *Chem. Soc. Rev.*, **2012**, *41*, 1111−1129.

(10) T. Ebina and F. Mizukami, *Adv. Mater.*, **2007**, *19*, 2450–2453.

(11) H. Tetsuka, T. Ebina, H. Nanjo, and F. Mizukami, *J. Mater. Chem.*, **2007**, *17*, 3545–3550.

(12) A. Isogai, T. Saito, and H. Fukuzumi, *Nanoscale*, **2011**, *3*,71−85.

(13) D. Klemm, F. Kramer, S. Moritz, T. Lindström, M. Ankerfors, D. Gray, and A. Dorris, *Angew. Chem., Int. Ed.*, **2011**, *50*, 5438−5466.

(14) T. Saito, S. Kimura, Y. Nishiyama, and A. Isogai, *Biomacromolecules*, **2007**, *8*, 2485-2491.

(15) Y. Okita, T. Saito, and A. Isogai, *Biomacromolecules*, **2010**, *11*, 1696–1700.

(16) H. Fukuzumi, T. Saito, T. Iwata, Y. Kumamoto, and A. Isogai, *Biomacromolecules*, **2009**, *10*, 162–165.

Chapter 2
Ultrastrong and high gas-barrier layered composites of nanocellulose and natural silicate

2.1 Introduction

Innovative development of biobased materials with high mechanical strengths and gas-barrier properties produced by environmentally friendly processes is highly desirable. Such materials are indispensable in, for example, lightweight transportation bodies, high-performance packages, and electronic devices in place of heavy steel or fiber-reinforced/petroleum-based materials in the building of a sustainable society. PLS nanocomposites are promising materials that meet the above needs. It has been shown that the mechanical and oxygen-barrier properties of polymeric materials can be improved by adding small amounts of MTM nanoplatelets (<10% w/w) to polymer matrices in the presence of a surfactant.[1−4]

Meanwhile, nanocelluloses or nanofibrillated celluloses (NFCs) have attracted increasing attention as new, biobased, and highly crystalline nanofibers because NFCs are not only environmentally compatible but also have unique characteristics as nanomaterials.[5] Preparations and characterizations of NFC-containing composites have been extensively studied in anticipation of high strength, high stiffness, biodegradability, lightweight, and other biobased functions.[6] In this context, multilayered organic/inorganic nanocomposites were prepared from NFC and MTM with a weight ratio of 50:50 to expect high strength and lightweight properties.[7] However, the Young's modulus, tensile strength, and strain-to-failure were lower than those of the neat NFC sheets in the absence of MTM.[8] These mechanical properties were probably caused by poor or no interaction between the partially aggregated nonionic NFC and the MTM, suggesting that better mechanical properties of NFC/MTM composites can be expected when NFCs with higher nano-dispersibility in water are used as the matrix component.

In the present study, we used TOCNs as the matrix component of PLS composites with MTM nanoplatelets. The TOCNs prepared in the present study have uniform widths of ~3 nm and an average length of ~1 μm.[9] Moreover, these TOCNs have anionic carboxylate groups on

the surfaces at a high density of ~1.4 groups nm^{-2}, so that electrostatic repulsions may effectively work not only between TOCNs but also between anionically charged MTM nanoplatelets and TOCNs in water.[10] Zeta potentials of TOCNs and MTM nanoplatelets were reported to be approximately −80 and −35 mV, respectively, in water at pH 7.[11,12] These electrostatic effects are expected to lead to sufficient nano-dispersibility of anionic MTM nanoplatelets in the anionic TOCN matrix. When MTM nanoplatelet is applied as a filler, highly intercalated or exfoliated states of MTM nanoplatelets in polymer matrices are required to achieve a high reinforcement effect.[13,14] In the present study, MTM nanoplatelets dispersed in water were prepared by simple mechanical agitation without using surfactant.

2.2 Experimental section

2.2.1 Materials

A softwood bleached kraft pulp was supplied by Nippon Paper Industries (Tokyo, Japan) in never-dried state with water content of 80%. MTM was supplied by Kunimine Industries and used without further chemical modification. Thickness and aspect ratios of the MTM nanoplatelets are approximately 1.1 nm and 200−400, respectively (see Chapter 4.3.1). The negative surface-charge content of the MTM is 1.15 mmol g^{-1}, according to the manufacturer. TEMPO, NaBr, a 2 M NaClO solution, and other chemicals were of laboratory grade (Wako Pure Chemicals, Osaka, Japan) and used as received.

2.2.2 TOCN dispersion

A TEMPO-oxidized cellulose was prepared from the wood cellulose according to the previously reported methods.[9,15−17] The cellulose (1g) was suspended in water (100 mL) containing TEMPO (0.016g, 0.1 mmol) and NaBr (0.1 g, 1 mmol). The 2M NaClO solution (1.9 mL, 3.8 mmol) was added to the cellulose/water slurry, and the mixture was stirred at room temperature and pH 10 until no 0.5 M NaOH consumption was observed. The TEMPO-oxidized cellulose thus obtained was further treated with 1% w/v $NaClO_2$ (100 mL) at pH 4.8 for 2 days to oxidize the C6-aldehyde groups remaining in the oxidized cellulose to carboxylate groups.[9,18] The two-step-oxidized cellulose had a carboxylate content of 1.21 mmol g^{-1}.[9,18] The TEMPO-oxidized cellulose/water slurry at a 0.11% w/v concentration was

mechanically treated with a double-cylinder type homogenizer for 1 min and subsequently with an ultrasonic homogenizer for 4 min.[9,15] The unfibrillated fraction (<15%) was removed by centrifugation at 12000g for 20 min. The supernatant was used as the TOCN dispersion, the concentration of which was adjusted to 0.1% w/v using a rotary evaporator under reduced pressure.

2.2.3 MTM nanoplatelet dispersion

MTM powder (0.6 g) was added to distilled water (30 mL) and agitated using a magnetic stirrer bar for 1 h. The 2% w/v MTM suspension thus prepared was mechanically treated by the same procedure as described above for the TOCN dispersion to improve dispersibility of MTM nanoplatelets in water. The MTM/water dispersion was stable and had no sedimentation even after 1 day. Turbidity of the MTM/water dispersion was measured using a JASCO V-670 UV-Vis spectrophotometer. Figure 2.1 shows that the turbidity of the MTM/water dispersion significantly decreases through the mechanical treatment.

2.2.4 TOCN/MTM composite films

The 2% MTM nanoplatelet dispersion was added to the 0.1% TOCN dispersion (30 g) at various weight ratios under stirring. After stirring for 1 h, the TOCN/MTM dispersion was poured in a polystyrene Petri dish with 50 mm diameter and oven-dried at 40 °C for 3 days. The TOCN/MTM composite film formed on the dish was peeled off and stored at 25 °C and 50% RH. The obtained TOCN/MTM composite films with weight ratios TOCN:MTM of 99:1, 95:5, 90:10, 75:25, and 50:50 were coded as TM01, TM05, TM10, TM25, and TM50, respectively.

2.2.5 Characterizations

Moisture contents of the films were determined from weight losses at 150 °C by thermogravimetric analysis using a Rigaku Thermoplus TG-8120. Light transmittance spectra of the films were measured using a JASCO V-670 UV-Vis spectrophotometer.[19,20] The film thickness was measured from at least five different positions for each sample using a Mitutoyo Series 227 digimatic micrometer and shown as a mean value. Standard deviation of film thickness was within 5% of the mean value. Tensile tests of the films were performed

using a Shimadzu EZ-TEST instrument equipped with a 500 N load cell at 23 °C and 50% RH. Rectangular strips 2 × 30 mm in size were cut from the films and tested with a span length of 10 mm at a rate of 1.0 mm min^{-1}. In tensile testing, at least 10 measurements were carried out for each sample. Young's modulus was determined from the slope of the initial linear region of the stress-strain curve. Yield stress was determined as the intersection of the tangents to the lines joining the initial elastic and the subsequent plastic curves. Work of fracture was calculated as the area below the stress-strain curve. Scanning electron microscope (SEM) observation of the film cross-sections was carried out with a Hitachi S4800 field-emission microscope equipped with an energy-dispersive X-ray (EDX) analyzer at 1 kV. The EDX spectra were recorded at 5.0 kV for 30 min. The samples subjected to SEM observation were coated with osmium using a Meiwafosis Neoc Osmium Coater at 10 mA for 5 s. X-ray diffraction (XRD) patterns of the films were obtained in reflection mode using a Rigaku RINT 2000 diffractometer with monochromator-filtered Cu Kα radiation (λ 0.15418 nm) at 40 kV and 40 mA. Oxygen permeabilities (P_{O2}) of the TOCN/MTM-coated poly(ethylene terephthalate) (PET) films were determined at 0% or 50% RH using a MOCON OX-TRAN Model 2/21 MH instrument according to a standard method (ASTM 3985).[21,22] Each sample was conditioned in the chamber for 3 h, and the oxygen transmission rates were measured for 50 cm^2 areas at atmospheric pressure over 1−3 days until a stable value was reached. The P_{O2} of the TOCN/MTM layer in the TOCN/MTM-coated PET film was calculated using the following equation,

$$\frac{T(\text{TOCN/MTM coated PET})}{P_{O2}(\text{TOCN/MTM coated PET})} = \frac{T(\text{TOCN/MTM})}{P_{O2}(\text{TOCN/MTM})} + \frac{T(\text{PET})}{P_{O2}(\text{PET})}$$

where T is thickness of the TOCN/MTM layer, PET film, or TOCN/MTM-coated PET film. Thicknesses of the TOCN/MTM layers and PET films were 1 μm and 50 μm, respectively.

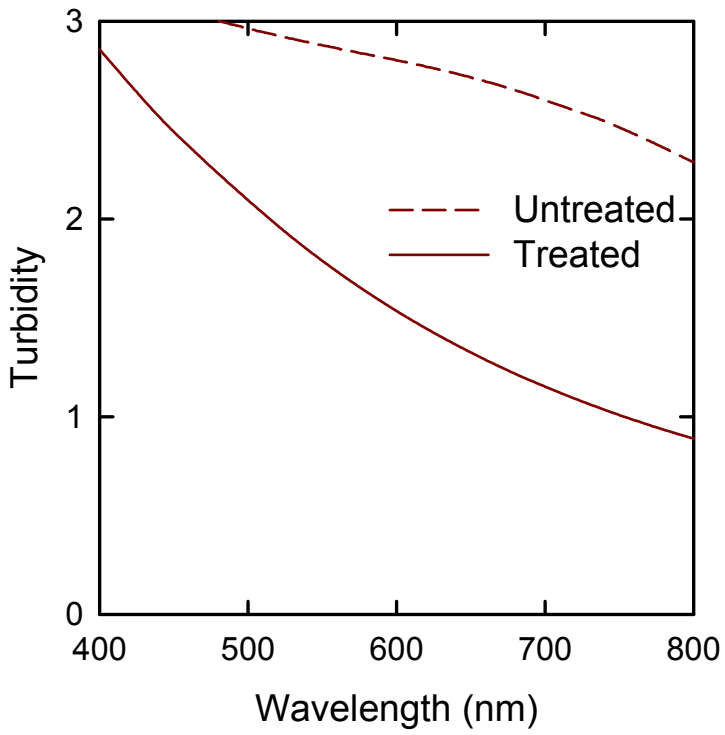

Figure 2.1. Turbidity of the untreated MTM dispersion (dashed line) and the MTM dispersion mechanically treated with a double-cylinder type homogenizer for 1 min and subsequently with an ultrasonic homogenizer for 4 min (solid line). Adapted with permission from Journal articles No.1 in Research achievement. © 2012 American Chemical Society.

2.3 Results and discussion

2.3.1 Optical properties

The TOCN/water and MTM/water dispersions were prepared separately, followed by mixing at various ratios, and TOCN/MTM composite films were prepared by cast-drying method. Figure 2.2a shows the light transmittances of the TOCN/MTM composite films. Thicknesses and densities of the films were 5−7.7 μm and 1.48−2.45 g cm^{-3}, respectively, and both of these values increased with MTM content. Moisture contents of the TOCN/MTM films at 23 °C and 50% RH were 5−9%. The Fabry−Perot fringes observed in Figure 2.2a indicate that the films had smooth surfaces.[19,23] The light transmittance of the TOCN/MTM films at 600 nm linearly decreased with increasing MTM content (Figure 2.2b). Figure 2.3 shows photographs of the flexible TOCN, TM05, TM50 films, and the neat MTM film. Therefore,

the TOCN/MTM composite films at 1−10% MTM contents are sufficiently flexible and transparent and their surfaces are smooth and glossy.

2.3.2 Structural analyses

Figure 2.4 shows SEM images of cross sections of the TOCN, neat MTM, TM05, and TM50 films. The nanofibril structures of TOCNs and sheet-like MTM stacks can be clearly observed in Figures 2.4a and 2.4b, respectively. The SEM image of the TM05 film (Figure 2.4c) reveals that distinct and closely-packed layered nanostructures were formed within the composites. The SEM image of the TM50 film (Figure 2.4d) shows more sheet-like and highly aligned structures of MTM nanoplatelets.[24–27] Therefore, the formation of layered nanostructures has been formed by embedding MTM nanoplatelets in TOCN matrix. Energy-dispersive X-ray (EDX) images (Figure 2.5) of cross sections of the TM50 film show that both the TOCNs and MTM nanoplatelets were homogeneously distributed in the film at the micron scale.

Figure 2.6 shows XRD patterns of the composites. The diffraction peak at around 7° corresponding to the interlayer spacing of MTM nanoplatelets became sharp with increasing MTM content of the composite. Thicknesses of the MTM aggregation or nanoplatelet stacks in the TOCN matrices, which were calculated from the full widths at half-maximum of the diffraction peaks, were substantially increased from 3−7.5 nm with increasing MTM content. The *d*-spacing, or interlayer spacing, of these MTM stacks decreased with increasing MTM content. These results suggest that more MTM nanoplatelets were aggregated during the process of drying the TOCN/MTM mixed dispersions with high MTM contents.

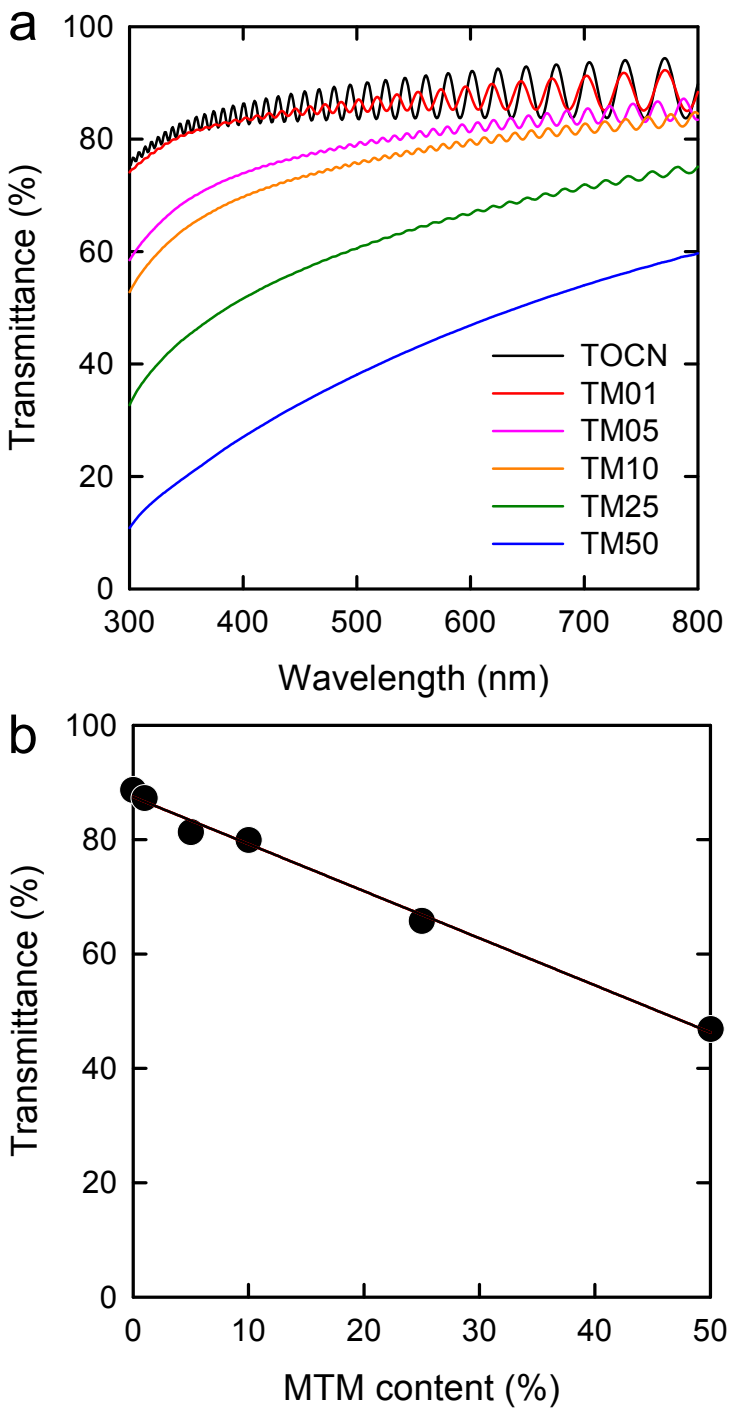

Figure 2.2. Light transmittances of the TOCN/MTM composite films with different MTM contents. (a) Light transmittances from 300 to 800 nm wavelength. (b) Light transmittances at 600 nm wavelength. Reprinted with permission from Journal articles No.1 in Research achievement. © 2012 American Chemical Society.

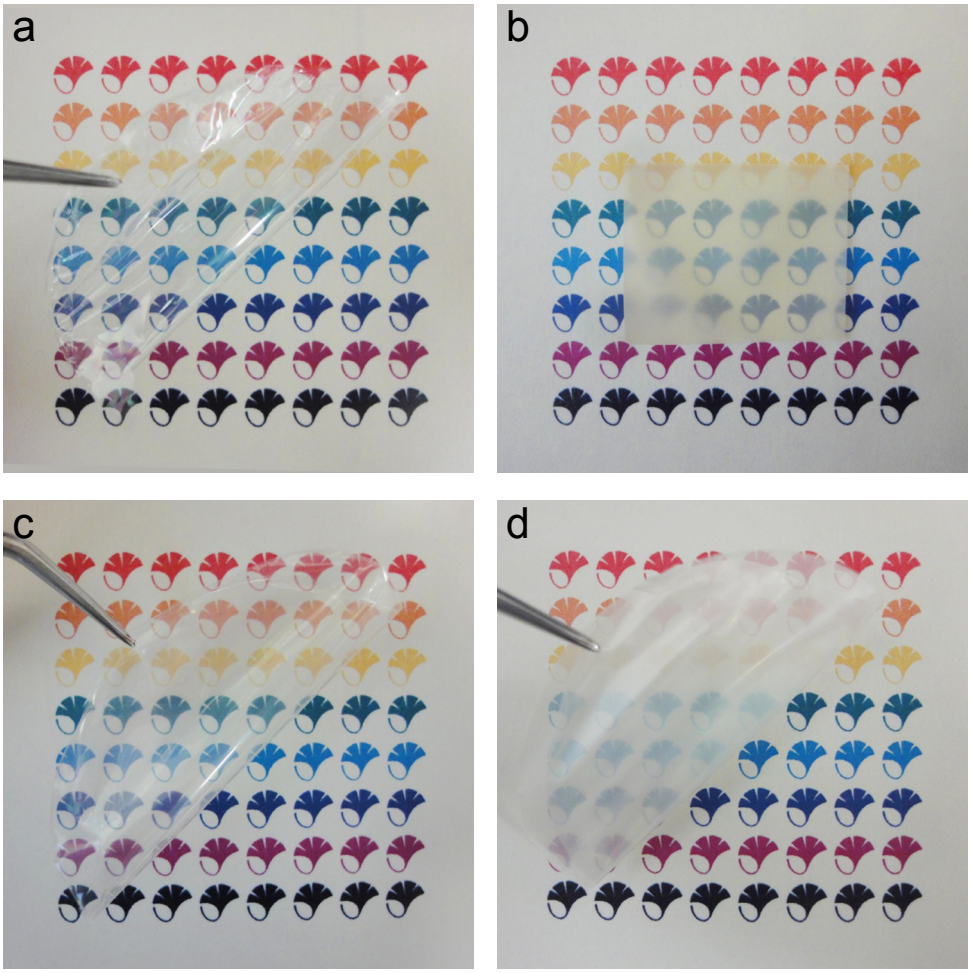

Figure 2.3. Photographs of the TOCN/MTM composite films with different MTM contents. (a, c, d) The flexible TOCN, TM05, and TM50 films. Thicknesses of the films were about 5−7.7 μm. (b) The neat MTM film with ~35 μm in thickness. Reprinted with permission from Journal articles No.1 in Research achievement. © 2012 American Chemical Society.

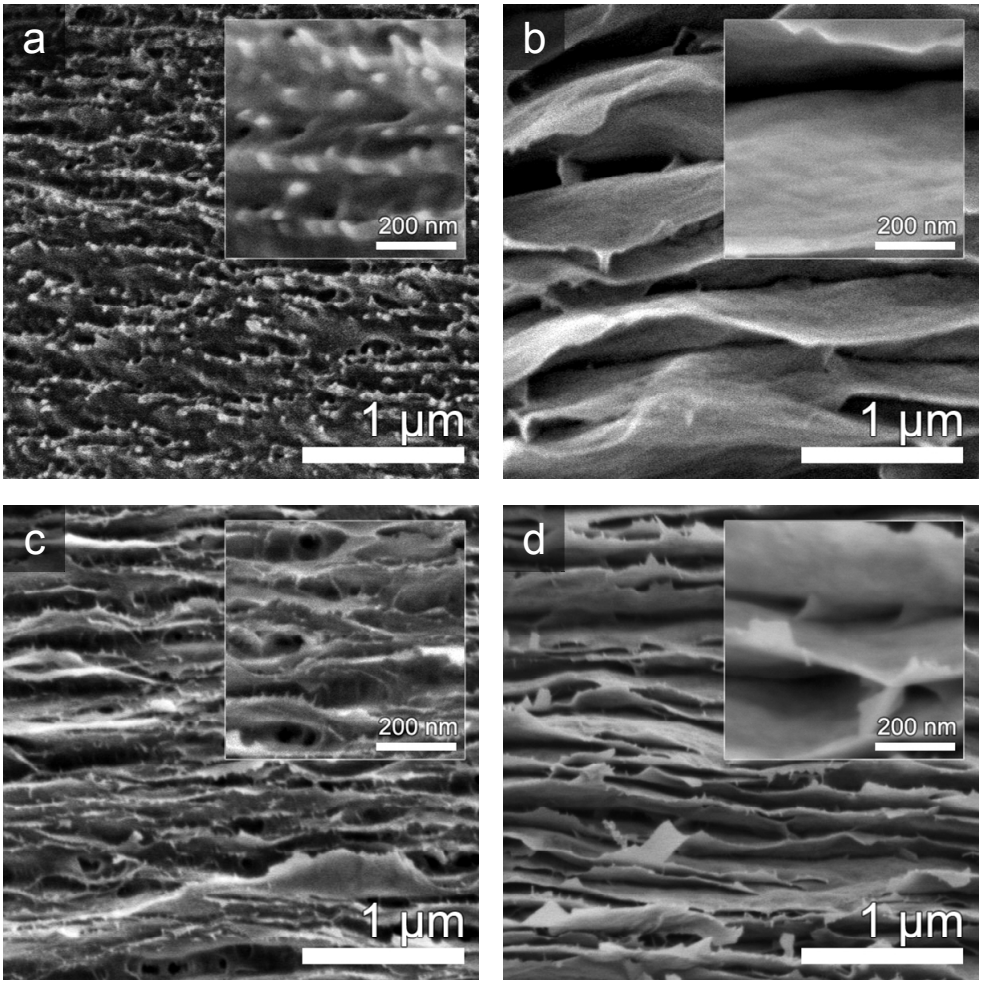

Figure 2.4. SEM images of the cross sections of the (a) TOCN, (b) neat MTM, (c) TM05, and (d) TM50 films. Reprinted with permission from Journal articles No.1 in Research achievement. © 2012 American Chemical Society.

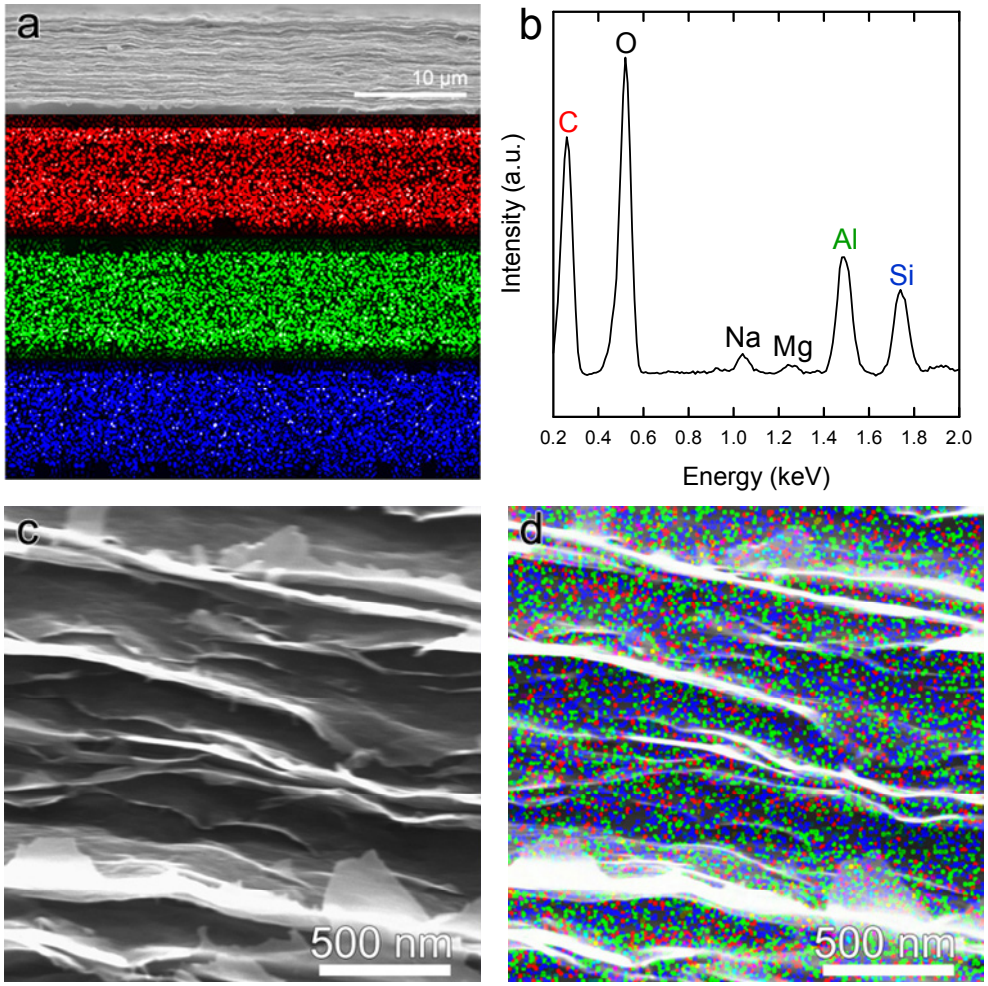

Figure 2.5. SEM-EDX results of the TM50 film (red: carbon, green: aluminum, blue: silicon). The EDX image (a) and spectrum (b) of the cross-section. The EDX images of the oblique close-up (c, d). Reprinted with permission from Journal articles No.1 in Research achievement. © 2012 American Chemical Society.

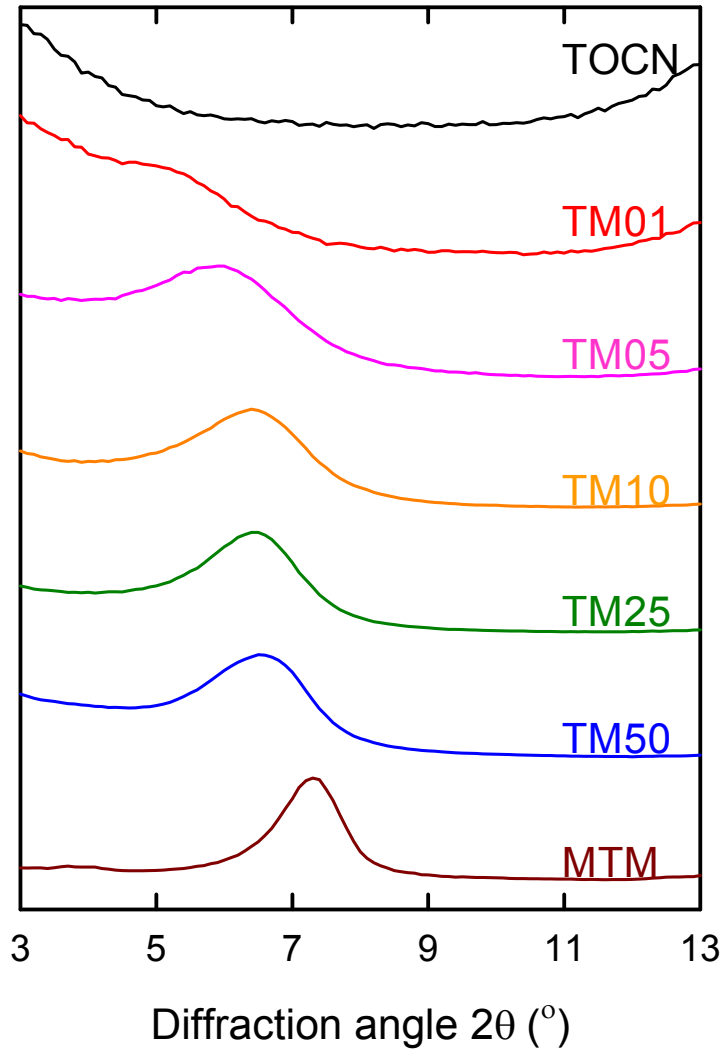

Figure 2.6. XRD patterns of the TOCN/MTM composite films with different MTM contents and the neat MTM film. Adapted with permission from Journal articles No.1 in Research achievement. © 2012 American Chemical Society.

2.3.3 Mechanical properties

Stress−strain curves, Young's moduli, tensile strengths, and strains-to-failure of the films are shown in Figure 2.7, and detailed data are listed in Table 2.1. The tensile test instrument used (Shimadzu EZ-TEST) was suitable for the thin TOCN/MTM composite films 5−7.7 μm in thickness to provide reliable data. The original TOCN film without MTM had a Young's modulus and a tensile strength of 11.6 GPa and 210 MPa, respectively. Mechanical properties of the TOCN film were significantly improved by combination with MTM nanoplatelets. The TM05 film had high Young's modulus of 18 GPa, ultrahigh tensile strength of 509 MPa, and high strain-to-failure of 7.6%, despite having a low density of 1.99 g cm^{-3}. Although the tensile strength and strain-to-failure had their maximum values for the TM05 film, Young's moduli had high levels >18 GPa for all composite films at 5−50% MTM content. The Young's modulus 18 GPa of TM05 indicated that each MTM nanoplatelet was discrete and fully functional as reinforcement. The possible interaction between the TOCNs and MTM nanoplatelets, and effective Young's modulus of MTM nanoplatelets in the TOCN matrix, or the modulus reinforcement efficiency, will be discussed in the next Chapter.

The high tensile strength of the TM05 film is similar to those of steels such as AISI 316 L and much higher than those of biobased organic/inorganic composite materials reported to date.[28,29] The strength reinforcement efficiency by MTM nanoplatelets in the TM05 film far exceeded those in the MTM-reinforced composite materials previously reported.[30−32] This high strength for the TM05 film is probably due to the homogeneous distribution of MTM nanoplatelets and favorable interactions at the interfaces between the TOCNs and MTM nanoplatelets (see Chapter 3.3.3 for the interactions). In addition, this high strength was combined with 7% strain-to-failure at only ~3% v/v of MTM phase, resulting in the significant improvement of work of fracture from 4 to 25 MJ m^{-3} (Figure 2.8). The work of fracture 25 MJ m^{-3} of the TM05 film is much higher than those of spring steels (1 MJ m^{-3}) and natural rubbers (10 MJ m^{-3}). When the neat MTM film was subjected to tensile testing, no data could be obtained because the film was too brittle.

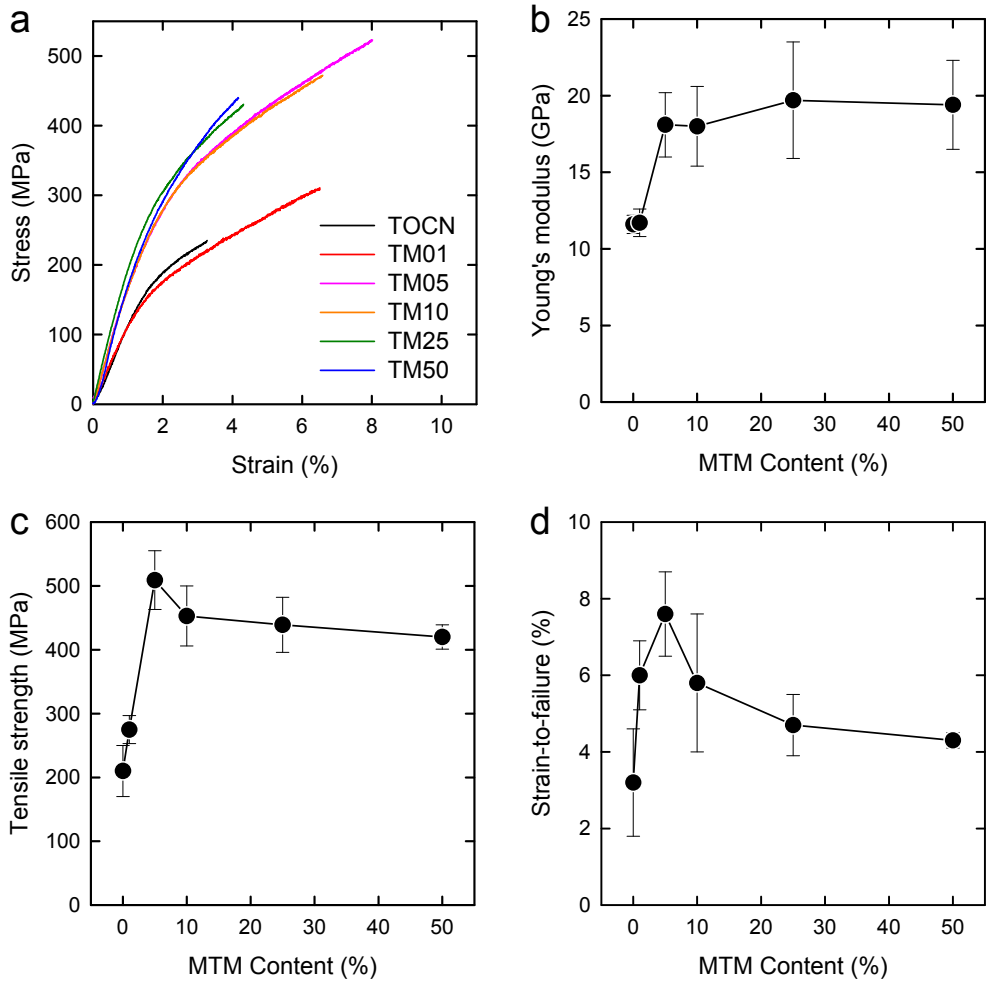

Figure 2.7. Mechanical properties of the TOCN/MTM films with different MTM contents. (a) Stress−strain curves. Note that the TM05 (pink) curve partially overlapped with the TM10 (orange) curve. (b) Young's moduli. (c) Tensile strengths. (d) Strains-to-failure. Adapted with permission from Journal articles No.1 in Research achievement. © 2012 American Chemical Society.

Table 2.1. Young's moduli, yield stresses, tensile strengths, strains-to-failure, and works of fracture of the TOCN/MTM composite films with different MTM contents. Adapted with permission from Journal articles No.1 in Research achievement. © 2012 American Chemical Society.

Sample	MTM content (wt %)	Young's modulus (GPa)	Yield stress (MPa)	Tensile strength (MPa)	Strain-to-failure (%)	Work of fracture (MJ m^{-3})
TOCN	0	11.6 ± 0.6	143 ± 27	210 ± 40	3.2 ± 1.4	4.2 ± 2.7
TM01	1	11.7 ± 0.9	161 ± 8	275 ± 22	6.0 ± 0.9	10.7 ± 1.9
TM05	5	18.1 ± 2.1	325 ± 21	509 ± 46	7.6 ± 1.1	25.6 ± 4.9
TM10	10	18.0 ± 2.6	298 ± 29	453 ± 47	5.8 ± 1.8	16.7 ± 6.3
TM25	25	19.7 ± 3.8	298 ± 24	439 ± 43	4.7 ± 0.8	13.5 ± 3.3
TM50	50	19.4 ± 2.9	265 ± 12	420 ± 19	4.3 ± 0.2	10.9 ± 0.2

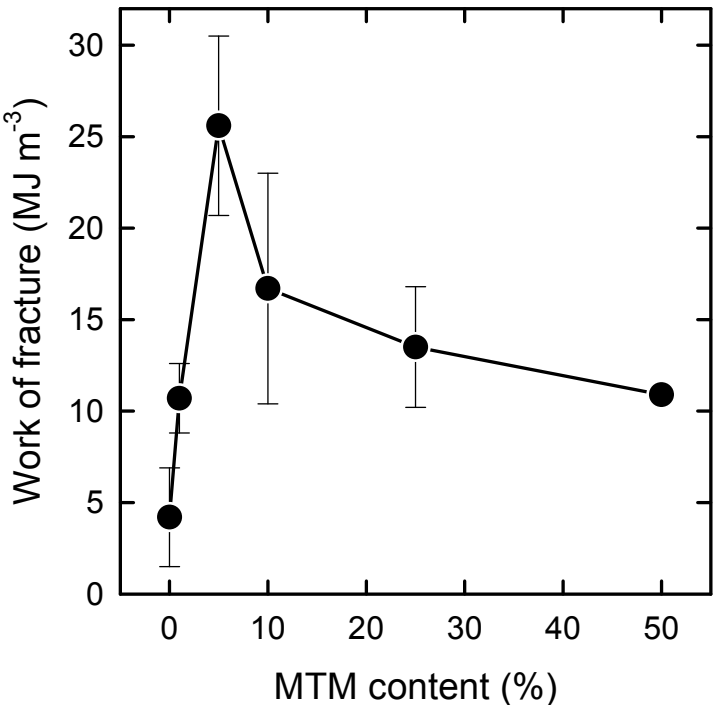

Figure 2.8. Works of fracture of the TOCN/MTM composite films. Adapted with permission from Journal articles No.1 in Research achievement. © 2012 American Chemical Society.

2.3.4 Oxygen-barrier properties

The oxygen permeability of the TOCN film at 0% RH markedly decreased from 0.03 to 0.007 mL μm m^{-2} day^{-1} kPa^{-1} with only 1% MTM addition (Figure 2.9). The TM50 film had an even lower value of 0.0008 mL μm m^{-2} day^{-1} kPa^{-1}. Therefore, the TOCN/MTM composite films showed excellent oxygen-barrier properties under dry conditions. The oxygen permeability of the TM50 film was markedly lower than those of commercial ethylene-vinylalcohol copolymer films (0.01 to 0.1 mL μm m^{-2} day^{-1} kPa^{-1}), which are commonly used as oxygen-barrier films.[24] Although the self-organized TOCN alignment in the neat TOCN film provide high oxygen-barrier properties at 0% RH, oxygen molecules could gradually pass through nanosized pores in the TOCN film.[21,22] The multi-walled structure formed by MTM nanoplatelets in the TOCN matrix (see Figure 2.4) should efficiently hinder oxygen permeation through the composite films, resulting in the significant improvement in oxygen-barrier property.

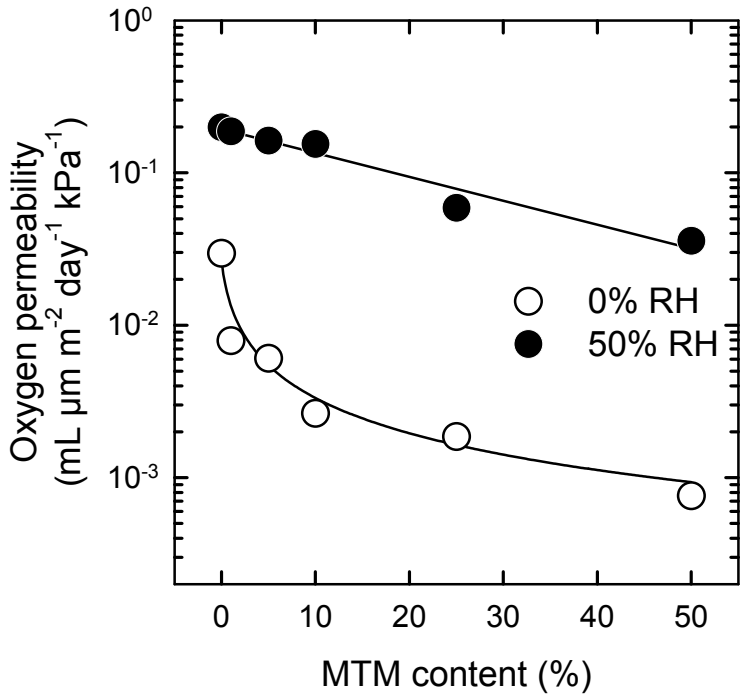

Figure 2.9. Oxygen permeabilities of the TOCN/MTM films with 0–50% MTM contents measured at 0 or 50% relative humidity. The thicknesses of the coated layers on poly(ethylene terephthalate) (PET) films were ~1 μm. Adapted with permission from Journal articles No.1 in Research achievement. © 2012 American Chemical Society.

However, the oxygen permeability of the TOCN film at 0% RH increased to 0.2 mL μm m^{-2} day^{-1} kPa^{-1} at 50% RH (Figure 2.9). This value clearly decreased with increasing MTM content in the composite films, and thus the MTM nanoplatelets contributed to improvement of oxygen-barrier properties even at 50% RH. Nevertheless, clear differences in oxygen permeability were still observed for the TOCN/MTM composite films between 0 and 50% RH, probably due to the hydrophilic nature of TOCNs and MTM nanoplatelets.

2.4 Conclusions

A new biobased PLS nanocomposite with excellent properties can be prepared from TOCNs and MTM nanoplatelets through a simple process of drying their water dispersions. The resulting TOCN/MTM composites have low densities of 1.5−2.5 g cm^{-3} yet show outstanding mechanical properties comparable to those of steels and very high oxygen-barrier properties. In particular, the composite films with 5% MTM content has ultrahigh tensile strength of 509 MPa and high Young's modulus of 18 GPa, which shows an unprecedentedly high reinforcement efficiency of organic matrix by MTM nanoplatelets. These characteristic properties are caused by 1) layered nanostructures of the TOCN/MTM composites, in which MTM nanoplatelets are in-plane oriented and homogeneously distributed in the TOCN matrix, and 2) forming numerous strong interactions at the interfaces between MTM nanoplatelets and TOCNs. Therefore, these TOCN/MTM composite films have numerous potential applications as new biobased PLS nanocomposites that are lightweight and possess ultrahigh mechanical strengths and high toughnesses. Energy efficiency in conversion processes from aqueous TOCN/MTM dispersions to dried nanocomposites should be improved in the future.

2.5 References

(1) T. D. Fornes, P. J. Yoon, H. Keskkula, and D. R. Paul, *Polymer*, **2001**, *42*, 9929−9940.

(2) H.-S. Lee, P. D. Fasulo, W. R. Rodgers, and D. R. Paul, *Polymer*, **2005**, *46*, 11673−11689.

(3) W. J. Choi, H.-J. Kim, K. H. Yoon, O. H. Kwon, and C. I. Hwang, *J. Appl. Polym. Sci.*, **2006**, *100*, 4875−4879.

(4) S. H. Kim and S. C. Kim, *J. Appl. Polym. Sci.*, **2007**, *103*, 1262−1271.

(5) D. Klemm, F. Kramer, S. Moritz, T. Lindström, M. Ankerfors, D. Gray, and A. Dorris, *Angew. Chem., Int. Ed.*, **2011**, *50*, 5438−5466.

(6) I. Siró and D. Plackett, *Cellulose*, **2010**, *17*, 459−494.

(7) H. Sehaqui, A. Liu, Q. Zhou, and L. A. Berglund, *Biomacromolecules*, **2010**, *11*, 2195−2198.

(8) A. Liu, A. Walther, O. Ikkala, L. Belova, and L. A. Berglund, *Biomacromolecules*, **2011**, *12*, 633−641.

(9) R. Shinoda, T. Saito, Y. Okita, and A. Isogai, *Biomacromolecules*, **2012**, *13*, 842−849.

(10) Y. Okita, T. Saito, and A. Isogai, *Biomacromolecules*, **2010**, *11*, 1696−1700.

(11) T. Saito, M. Hirota, N. Tamura, S. Kimura, H. Fukuzumi, L. Heux, and A. Isogai, *Biomacromolecules*, **2009**, *10*, 1992−1996.

(12) T. Yoshida and M. Suzuki, *Colloids Surf. A*, **2008**, *325*, 115−119.

(13) A. Walther, I. Bjurhager, J. M. Malho, J. Pere, J. Ruokolainen, L. A. Berglund, and O. Ikkala, *Nano Lett.*, **2010**, *10*, 2742−2748.

(14) D. R. Paul and L. M. Robeson, *Polymer*, **2008**, *49*, 3187−3204.

(15) T. Saito, Y. Nishiyama, J. L. Putaux, M. Vignon, and A. Isogai, *Biomacromolecules*, **2006**, *7*, 1687−1691.

(16) T. Saito, S. Kimura, Y. Nishiyama, and A. Isogai, *Biomacromolecules*, **2007**, *8*, 2485−2491.

(17) A. Isogai, T. Saito, and H. Fukuzumi, *Nanoscale*, **2011**, *3*, 71−85.

(18) T. Saito and A. Isogai, *Biomacromolecules*, **2004**, *5*, 1983−1989.

(19) Z.-D. Qi, T. Saito, Y. Fan, and A. Isogai, *Biomacromolecules*, **2012**, *13*, 553−558.

(20) T. Saito, T. Uematsu, S. Kimura, T. Enomae, and A. Isogai, *Soft Matter*, **2011**, *7*, 8804−8809.

(21) H. Fukuzumi, T. Saito, S. Iwamoto, Y. Kumamoto, T. Ohdaira, R. Suzuki, and A. Isogai, *Biomacromolecules*, **2011**, *12*, 4057−4062.

(22) H. Fukuzumi, T. Saito, T. Iwata, Y. Kumamoto, and A. Isogai, *Biomacromolecules*, **2009**, *10*, 162−165.

(23) M. Takahashi, K. Iyoda, T. Miyauchi, S. Ohkido, M. Tahashi, K. Wakita, N. Kajitani, M. Kurachi, and K. Hotta, *J. Appl. Phys.*, **2009**, *106*, 044102.

(24) J. Lange and Y. Wyser, *Packag. Technol. Sci.*, **2003**, *16*, 149−158.

(25) B. Long, C.-A. Wang, W. Lin, Y. Huang, and J. Sun, *Compos. Sci. Technol.*, **2007**, *67*, 2770−2774.

(26) R. Chen, C.-A. Wang, Y. Huang, and H. Le, *Mater. Sci. Eng., C*, **2008**, *28*, 218−222.

(27) H. B. Yao, Z. H. Tan, H. Y. Fang, and S. H. Yu, *Angew. Chem., Int. Ed.*, **2010**, *49*, 10127−10131.

(28) J. Wang, Q. Cheng, and Z. Tang, *Chem. Soc. Rev.*, **2012**, *41*, 1111−1129.

(29) C.-M. Tseng, H.-Y. Liou, and W.-T. Tsai, *Mater. Sci. Eng., A*, **2003**, *344*, 190−200.

(30) Z. Tang, N. A. Kotov, S. Magonov, and B. Ozturk, *Nat. Mater.*, **2003**, *2*, 413−418.

(31) P. Podsiadlo, A. K. Kaushik, E. M. Arruda, A. M. Waas, B. S. Shim, J. Xu, H. Nandivada, B. G. Pumplin, J. Lahann, A. Ramamoorthy, and N. A. Kotov, *Science*, **2007**, *318*, 80−83.

(32) E. Munch, M. E. Launey, D. H. Alsem, E. Saiz, A. P. Tomsia, and R. O. Ritchie, *Science*, **2008**, *322*, 1516−1520.

Chapter 3
Highly tough and transparent layered composites of nanocellulose and synthetic silicate

3.1 Introduction

For material properties of PLS nanocomposites, knowledge of the aspect ratio, or the ratio of the platelet size to the thickness, of silicate nanoplatelets is important.[1] High-aspect-ratio nanoplatelets of a high surface area can achieve both a high stress transfer from the polymer matrix to the nanoplatelets and a high barrier to gas diffusion, leading to dramatic improvement in the mechanical, thermal, and gas-barrier properties. To realize these improvements, the nanoplatelets must be oriented parallel to the loading direction, or perpendicular to the gas-diffusion direction, and have favorable interactions at the polymer matrix interface. Polymer composites reinforced with high-aspect-ratio nanoplatelets exhibit high strength but are relatively brittle. In contrast, the composites reinforced with low-aspect-ratio nanoplatelets have lower strength than those with higher aspect ratios, but are more ductile and tough. These properties can be explained based on models of PLS composite fracture behaviour (Figure 3.1);[1,2] high-aspect-ratio platelets of high surface area can accept sufficient interfacial shear stress to be fractured in the composite, while low-aspect-ratio platelets of low surface area are pulled out from the polymer matrix under the same loading conditions, allowing the composites to strain more. In addition, the aspect ratio and dispersibility of silicate nanoplatelets are often in a reciprocal relationship; low-aspect-ratio nanoplatelets are dispersed better than high-aspect-ratio ones.

Here, we report a highly tough and transparent PLS nanocomposite prepared from synthetic low-aspect-ratio SPN nanoplatelets and TOCNs. We show that the advantages of using low-aspect-ratio nanoplatelets can be fully realized using TOCNs as the polymer component.

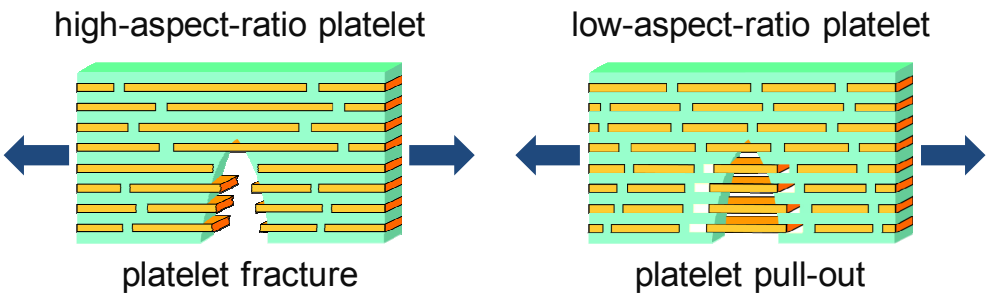

Figure 3.1. Fracture mechanisms of PLS nanocomposites reinforced with high- or low-aspect-ratio platelets.[1]

3.2 Experimental section

3.2.1 Materials

A softwood bleached kraft pulp in a never-dried state (water content 80%) was supplied by Nippon Paper Industries (Tokyo, Japan). For demineralization, the pulp was stirred in a diluted HCl solution at pH ~2.5 for 2 h and washed with deionized water by filtration. A synthetic SPN in powder form was supplied by Kunimine Industries (Tokyo, Japan). The platelet size of the SPN nanoplatelets is ~50 nm, and the surface negative charge and edge positive charge densities are ~1.0 mmol g^{-1} and ~0.1 mmol g^{-1}, respectively, according to the manufacturer. Other chemicals were purchased from Wako Pure Chemicals (Osaka, Japan) and used as received.

3.2.2 TOCN dispersion

See Chapter 2.2.2.

3.2.3 SPN nanoplatelet dispersion

SPN powder (0.6 g) was incrementally added to distilled water (30 mL) under stirring. After 1 h, the 2% w/v SPN suspension was treated with a double-cylinder-type homogenizer (Physcotron NS-56; Microtec) for 1 min and subsequently with an ultrasonic homogenizer (US-300T; Nihon Seiki) for 4 min. The resulting dispersion of SPN nanoplatelets was optically transparent and highly viscous (Figure 3.2).

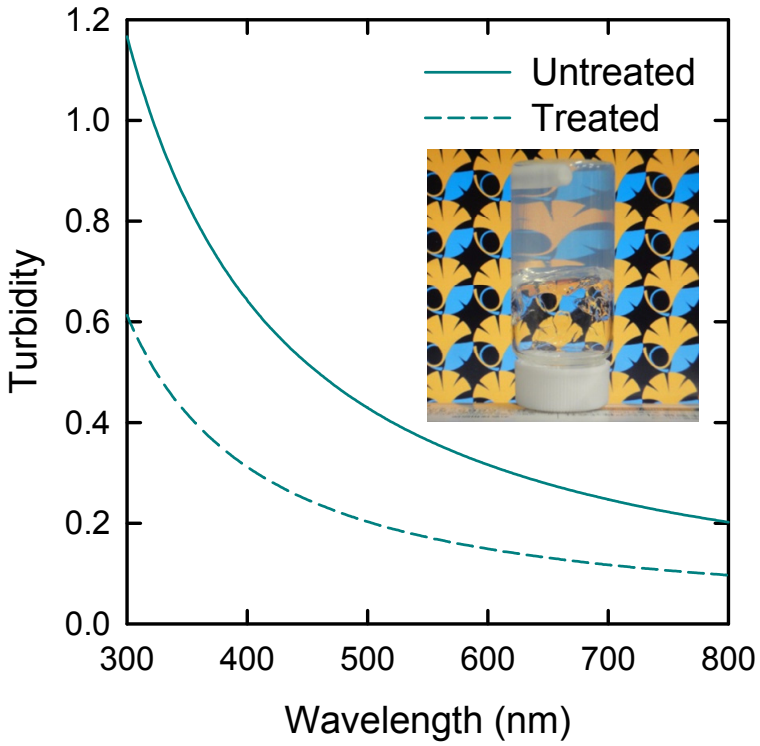

Figure 3.2. Turbidities of 2% w/v SPN dispersions before and after homogenizing treatments using a mechanical homogenizer of double-cylinder type and an ultrasonic homogenizer. The inset is a photograph of the homogenized SPN dispersion standing upside down, showing transparency and high viscosity of the dispersion. Reproduced from Journal articles No.2 in Research achievement with permission from The Royal Society of Chemistry.

3.2.4 TOCN/SPN composite films

The method is the same as that described in Chapter 2.2.4. The TOCN/SPN composite films with TOCN:SPN weight ratios of 99:1, 95:5, 90:10, 75:25, and 50:50 were coded as TS01, TS05, TS10, TS25, and TS50, respectively.

3.2.5 Characterizations

Moisture contents, light transmittance spectra, and thicknesses of the films were measured by the same methods as that described in Chapter 2.2.5. Tensile tests, Scanning electron microscope (SEM) observation, energy-dispersive X-ray (EDX) analyses, and X-ray diffraction (XRD) analyses were carried out by the same methods as that described in Chapter 2.2.5. Oxygen permeabilities of the TOCN/SPN-coated poly(ethylene terephthalate) (PET)

films were determined by the same methods as that described in Chapter 2.2.5.

3.3 Results and discussion

3.3.1 Optical properties

The TOCN/SPN composite films were prepared by cast-drying mixed dispersions of TOCNs and SPN nanoplatelets. The SPN content in the composites varied from 1% to 50% w/w by controlling the mixing ratios. Thicknesses of the films increased as the amount of added SPN dispersion was increased, and were 5.0–11.7 μm. Densities and moisture contents of the composite films at 23 °C and 50% RH were 1.5–2.0 g cm^{-3} and 7–10% w/w, respectively. The density linearly increased with SPN content. Assuming the true densities of the TOCNs and SPN nanoplatelets to be 1.6 g cm^{-3} and 2.8 g cm^{-3}, respectively, porosities of all the composite films are less than 5%, regardless of SPN content. These low porosities suggest dense packing of TOCNs and SPN nanoplatelets in the composites.

Figure 3.3 shows light transmittance spectra of the TOCN/SPN composite films. All the composite films with 1–50% SPN content were transparent. The transmittance spectra showed the Fabry-Perot interference over a wide range of wavelengths, indicating that the composite films have flat and smooth reflecting surfaces. These transparent composite films were flexible (Figure 3.4a−c) and even foldable (Figure 3.4d). It should be noted that even the composite film with a high 50% w/w SPN content is transparent and foldable. In general, the optical transparency of polymer nanocomposites reinforced with high-aspect-ratio silicates such as MTM significantly decreases with increasing silicate content (see Figure 2.2 and 2.3).

3.3.2 Structural analyses

Figure 3.5 shows SEM images of cross-sections of the neat TOCN, TS10, TS50, and neat SPN films. Both the neat TOCN film (Figure 3.5a) and the neat SPN film (Figure 3.5b) have layered structures; the layered structures in the TOCN film are composed of in-plane oriented nanofibrils,[3,4] while those in the SPN film are composed of nanoplatelet stacks. Layered structures were also observed in the composite films (Figures 3.5c and 3.5d). These layers were oriented parallel to the film surfaces. The layered structures in the composite become sharply defined and plate-like with increasing SPN content. Similar layered structures have

been observed for composites of MTM nanoplatelets and cellulose nanofibrils.[5] The layered structures in the TOCN/SPN composites are more finely segregated than those in the cellulose/MTM composites (see Figure 2.4). Elemental mapping of the film cross-sections by EDX (Figures 3.5e and 3.5f) showed that the SPN nanoplatelets are homogeneously distributed within the composites at the micron scale. Furthermore, XRD analyses of the TOCN/SPN composites showed that SPN nanoplatelets in the composites with low SPN content are highly dispersed in the TOCN matrix at the nanometer scale (Figure 3.6); the (001) diffraction of SPN nanoplatelets, corresponding to the inter-platelet spacing of the nanoplatelets, was undetected for the TS01, TS05, and TS10. The broad (001) diffraction pattern for the TS25 and TS50 indicates that a part of SPN nanoplatelets are aggregated in the composites. These aggregations in TS25 and TS50 were likely formed when the water dispersions with high SPN contents of 25–50% were dried.

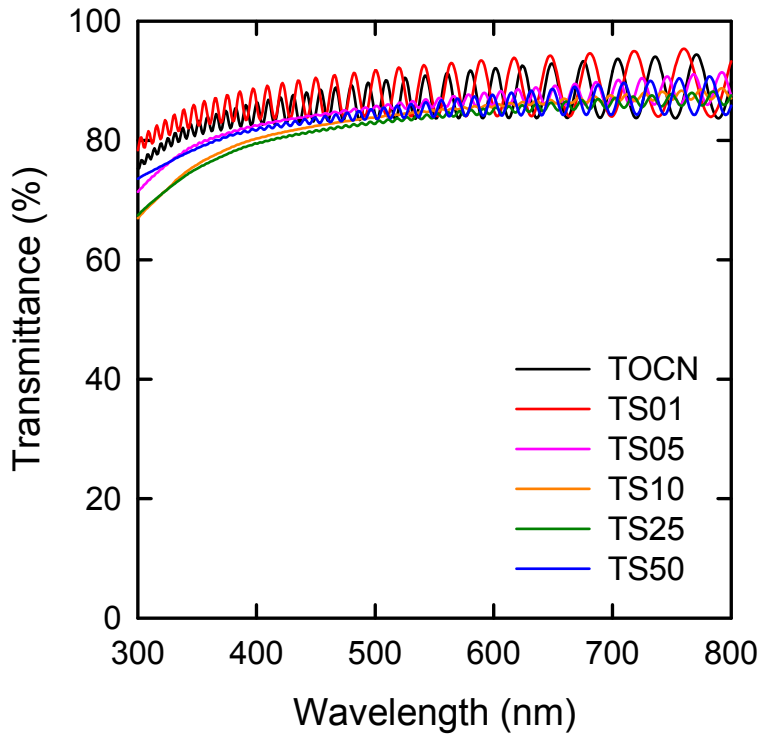

Figure 3.3. Light transmittance of the TOCN/SPN composites with 0–50% w/w SPN contents. Reproduced from Journal articles No.2 in Research achievement with permission from The Royal Society of Chemistry.

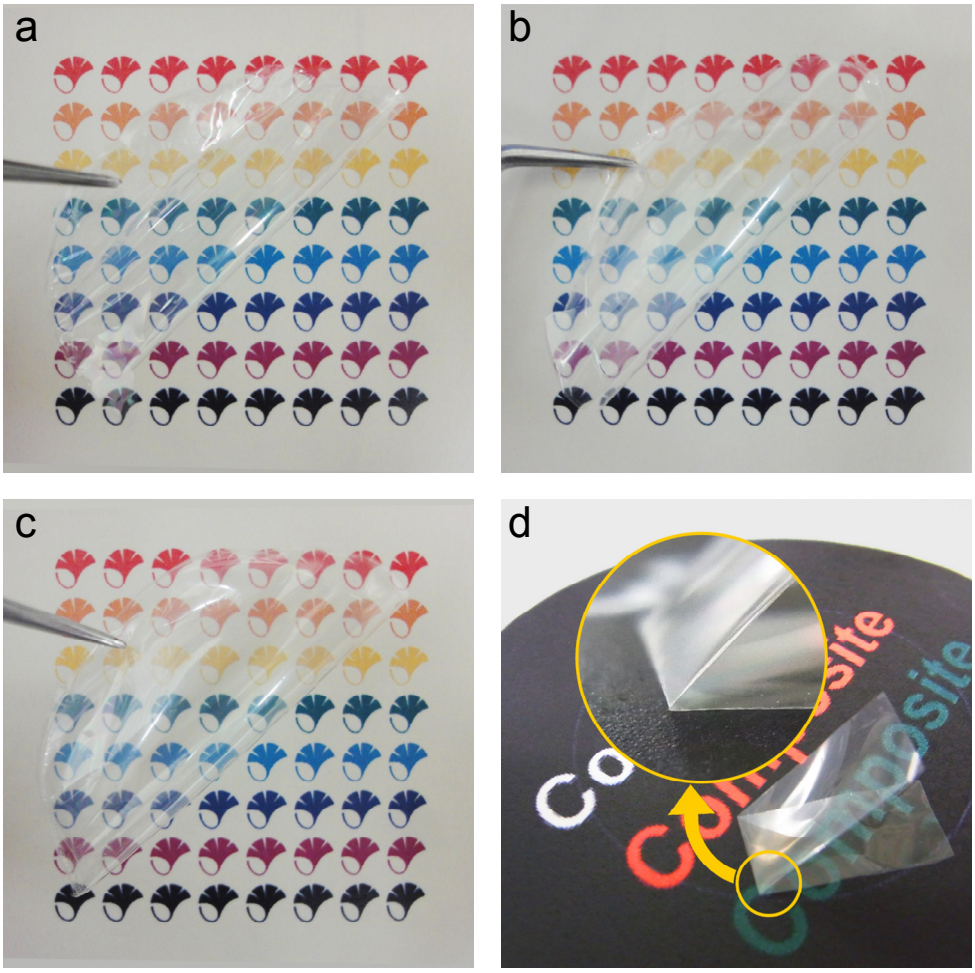

Figure 3.4. Flexible transparent films of the (a) neat TOCN, (b) TS10, and (c) TS50. (d) A folded film of TS50. Reproduced from Journal articles No.2 in Research achievement with permission from The Royal Society of Chemistry.

3.3.3 Mechanical properties

Mechanical properties of the TOCN/SPN composites varied depending on the SPN content. Tensile properties of the composites are shown in Figure 3.7, and detailed data are listed in Table 3.1. All the stress-strain curves showed similar trends; the linear elastic region was observed until a strain of 0.5–1%, and at a higher strain, strong strain-hardening was observed in the plastic region. The Young's modulus and yield stress of the composites increased almost linearly with increasing SPN content up to 25% and 10%, respectively, after which these values reached a plateau. This result indicated that the energy required for reaching the yield stress or the maximum elastic strain energy increased with increasing SPN content up to

10%, and then decreased. The yielding was probably caused by interfacial slippage of TOCNs and SPN nanoplatelets in the composite.[3] Tensile strength, strain-to-failure, and work of fracture of the composite also increased with increasing SPN content up to 10% and then decreased. All the composites showed similar strain-hardening in the plastic region, so that the tensile strength of the TOCN/SPN composites is correlated with strain-to-failure. The decrease in mechanical properties at the SPN contents of over 10% is probably due to aggregation of SPN nanoplatelets within the composites, as indicated in the XRD analyses of TS25 and TS50 (Figure 3.6).

The TOCN/SPN composite with SPN content 10% (TS10) showed a unique combination of Young's modulus (14.5 GPa), tensile strength (425 MPa), and strain-to-failure (10.2%). As a result, work of fracture of the TS10 is as high as 30 MJ m^{-3}. The tensile strength of TS10 is comparable to that of some steels, while the modulus is one order of magnitude lower than those of the steels, revealing that the TOCN/SPN composite has a great advantage over the steels in terms of flexibility. The work of fracture of 4.2 MJ m^{-3} of neat TOCN films increased by more than 7-fold as the SPN content was increased to 10% w/w. This increase in the work of fracture for the TOCN/SPN composites is outstanding, and is, to our knowledge, higher than those for a range of the PSL nanocomposites reported to date. In the previous study, we prepared a PLS nanocomposite from TOCNs and MTM nanoplatelets. The TOCN/MTM composite with MTM content 5% w/w showed an excellent mechanical performance of Young's modulus of 18 GPa, tensile strength of 509 MPa, strain-to-failure of 7.6%, and work of fracture of 25.6 MJ m^{-3}. The TOCN/SPN composite prepared in the present study showed lower values for modulus and strength, yet higher values for strain-to-failure and work of fracture than the TOCN/MTM composite. The high work of fracture of the TOCN/SPN composites can be interpreted based on a model for fracture of polymer composites reinforced with low-aspect-ratio platelets (see Chapter 3.1); the low-aspect-ratio SPN nanoplatelets embedded in the TOCN matrix were pulled out from the matrix, so that the composite strained more and displayed a higher work of fracture. Although transparent SPN-based PLS nanocomposites have been reported,[6,7] mechanical properties of those nanocomposites are inferior to the TOCN/SPN composites prepared in the present study.

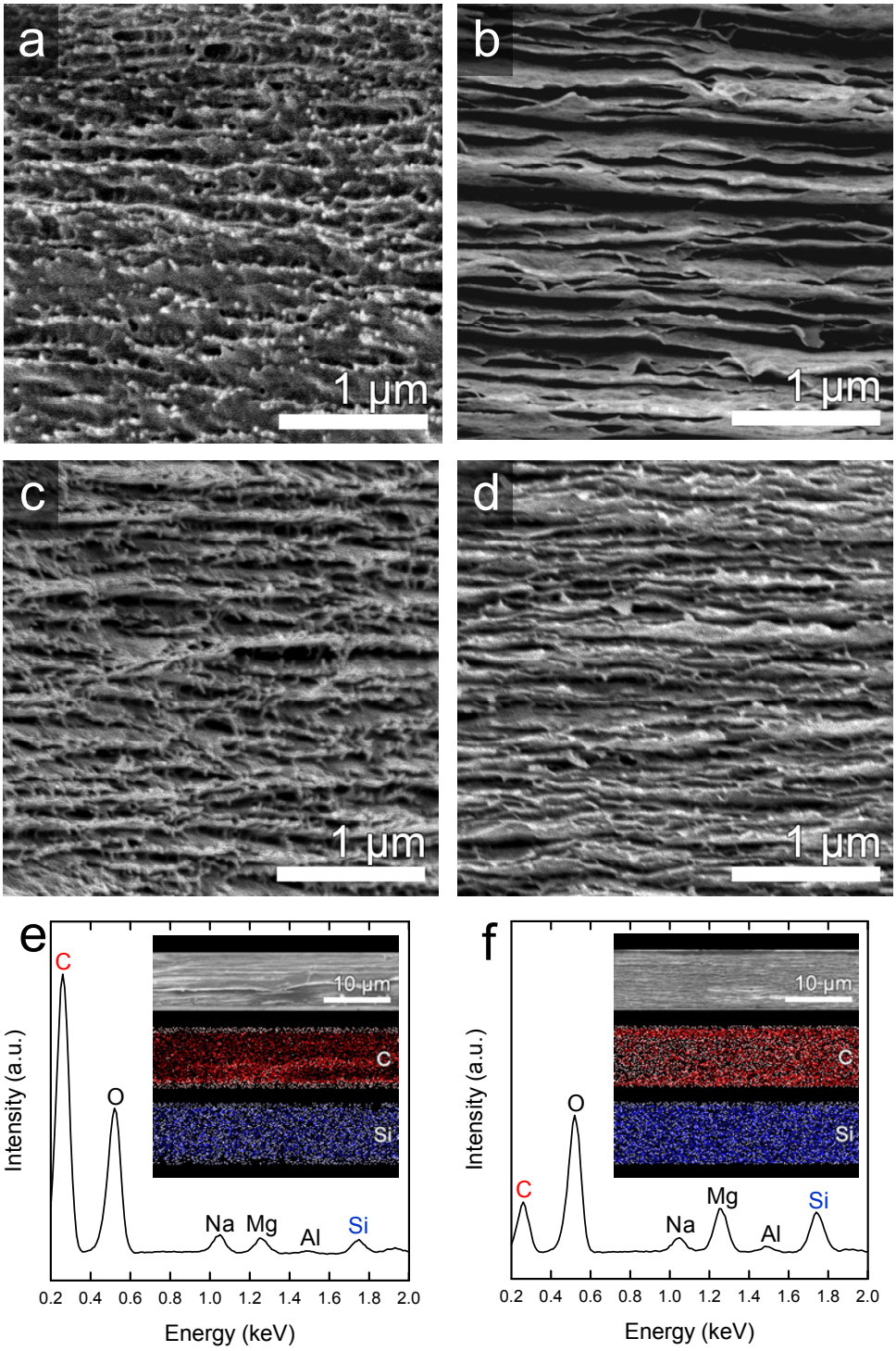

Figure 3.5. SEM images of the cross-sections of (a) neat TOCN, (b) neat SPN, (c) TS10, and (d) TS50 films. SEM-EDX spectra of the film cross-sections for (e) TS10 and (f) TS50. The insets show whole images of the film cross-sections and the elemental mapping of carbon (TOCNs) and silicon (SPN). Reproduced from Journal articles No.2 in Research achievement with permission from The Royal Society of Chemistry.

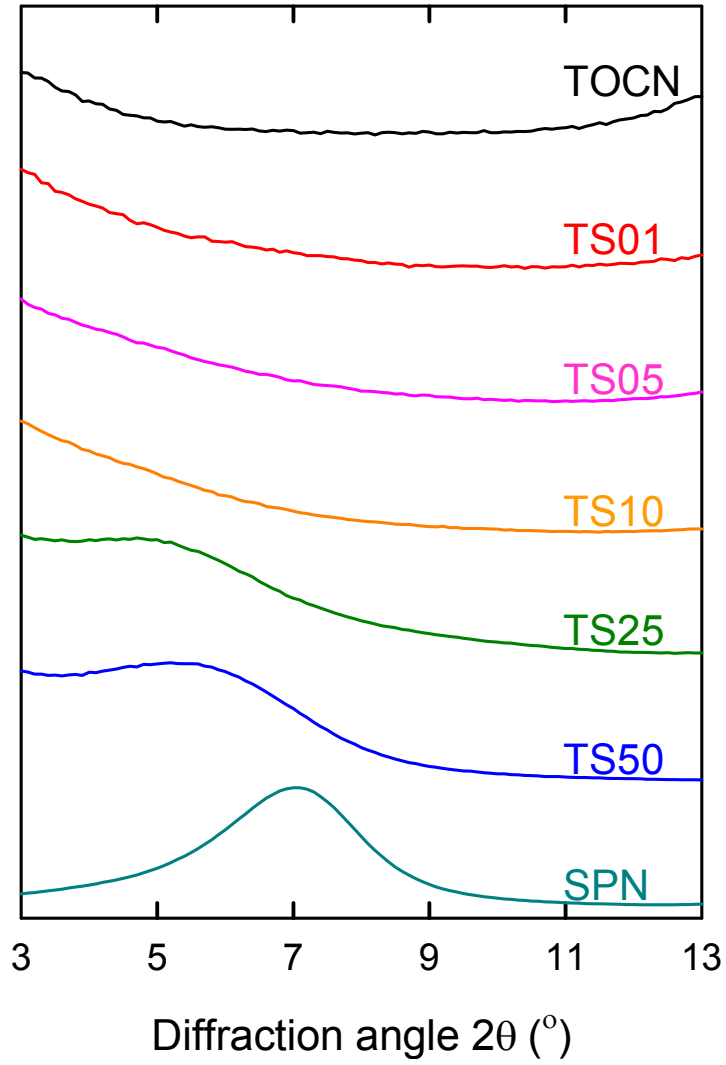

Figure 3.6. XRD patterns of the neat TOCN, TOCN/SPN composites, and neat SPN films, showing changes in the (001) diffraction of SPN nanoplatelets as a function of SPN content in the composites. Adapted from Journal articles No.2 in Research achievement with permission from The Royal Society of Chemistry.

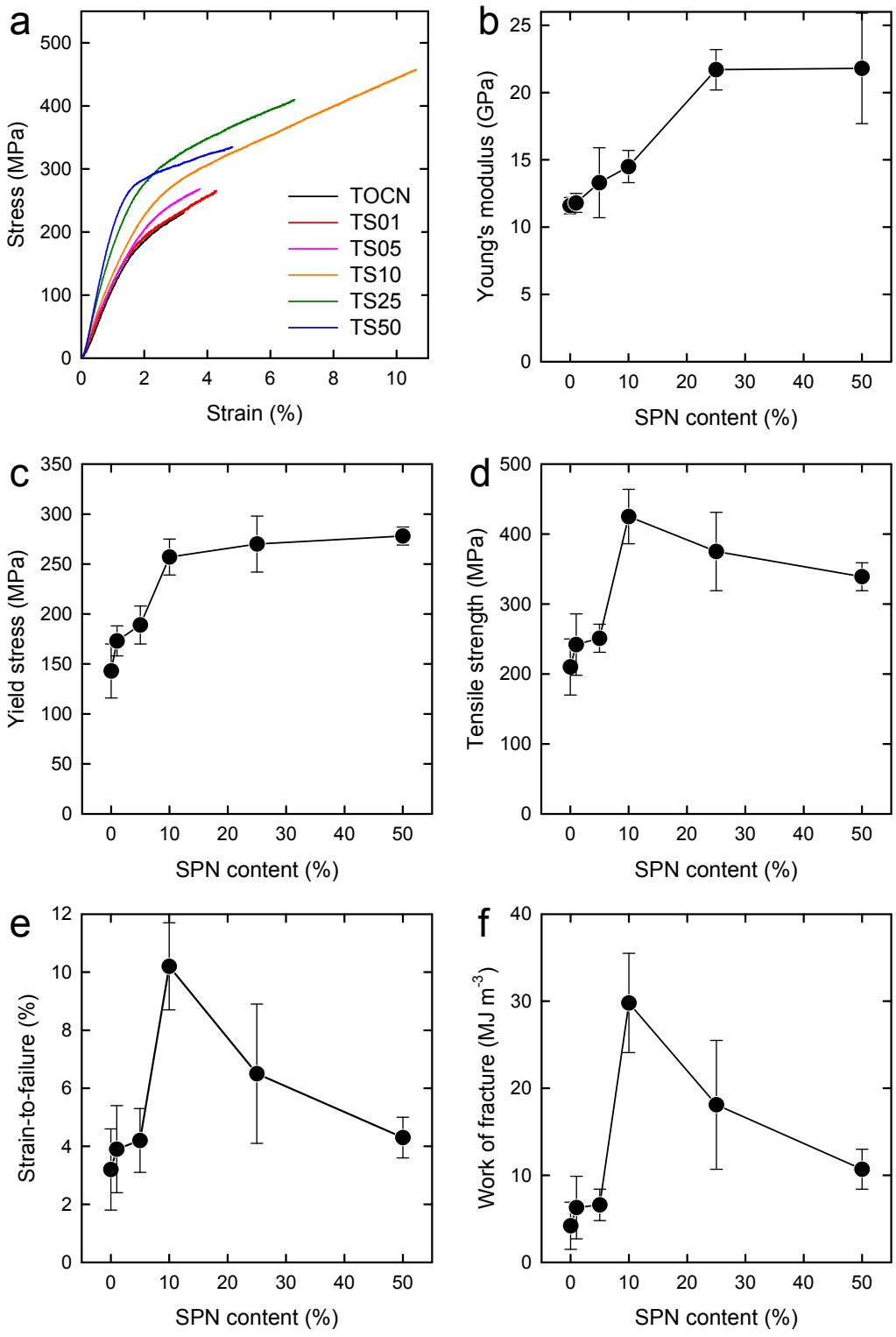

Figure 3.7. Mechanical properties of the TOCN/SPN composite films with SPN content 0–50% w/w: (a) stress-strain curve, (b) Young's modulus, (c) yield stress, (d) tensile strength, (e) strain-to-failure, and (f) work of fracture. Reproduced from Journal articles No.2 in Research achievement with permission from The Royal Society of Chemistry.

The reinforcement efficiency of the SPN nanoplatelets embedded in the TOCN matrix was assessed by calculating the effective Young's modulus and tensile strength of the SPN nanoplatelets (Figure 3.8). Young's modulus E_c of the polymer composites reinforced with low-aspect-ratio silicates is estimated using the following equation,[8,9]

$$E_c = \alpha E_r V_r + E_s(1 - V_r)$$

where E_r and E_s are the Young's moduli of the silicate platelets and polymer matrix, respectively, V_r is the volume fraction of the silicate platelets, and α is an empirical efficiency factor. The factor α is described as follows,

$$\alpha = \left[1 - \frac{\tanh(u)}{u}\right]$$

where

$$u = p\sqrt{\frac{V_r E_s}{2E_r(1 - V_r)(1 + \nu)}}$$

where p is the aspect ratio of the silicate platelets, and ν is the Poisson's ratio of the polymer matrix. In this prediction, the silicate platelets in the composite are assumed to orient parallel to the loading direction and have ideal interactions with the polymer matrix. In the present study, a Young's modulus of 11.6 GPa for the neat TOCN films and an aspect ratio of 50 for the SPN nanoplatelets were applied to E_s and p, respectively, Poisson's ratio ν of the TOCN matrix was assumed to be –0.1,[10] and the volume fraction V_r was calculated assuming densities of the TOCN matrix and SPN nanoplatelets to be 1.5 g cm^{-3} and 2.8 g cm^{-3}, respectively. Figure 3.8a shows the best fitting of the estimated modulus E_c to the experimental values. This fitting was obtained when the modulus E_r of the nanoplatelets was 100 GPa; in fact, the effective Young's modulus of the SPN nanoplatelets in TOCN/SPN composites was estimated to be 100 GPa. The effective modulus value of 100 GPa for the SPN nanoplatelets is lower than that for the MTM nanoplatelets in the TOCN/MTM

composite (250 GPa), but is the same as the value reported for MTM nanoplatelets embedded in a xyloglucan matrix, one of the PLS nanocomposite systems that displays the highest modulus reinforcement efficiencies.[11] It is significant that an effective modulus of 100 GPa was obtained without covalent cross-linking between the polymer matrix and the silicate platelets.[12,13]

Conversely, the tensile strength σ_c of polymer composites reinforced with low-aspect-ratio silicates can be estimated using the following equation,[1,2]

$$\sigma_c = \beta\sigma_r V_r + \sigma_s(1 - V_r)$$

where σ_r and σ_s are the tensile strengths of the silicate platelets and polymer matrix, respectively, and β is an empirical efficiency factor. The factor β is described as follows,

$$\beta = \frac{\tau_y p}{2\sigma_r}$$

where τ_y is the yield shear strength of the polymer matrix. In this prediction, the polymer matrix in the PLS composite is assumed to yield before the platelets break, and the composites fail under the platelet-pull-out mode. In the present study, the tensile and yield strengths of 210 MPa and 143 MPa, respectively, of the TOCN matrix were used for σ_s and τ_y, and the volume fraction V_r and aspect ratio p of the SPN nanoplatelets were set as the same values as those used in the modulus calculations. As a result, the strength of TOCN/SPN composites was well described by this fracture model of platelet-pull-out mode (Figure 3.8b).

The high reinforcement efficiency of the silicate nanoplatelets suggests the presence of favorable interactions between the TOCNs and silicate nanoplatelets in the composites. No covalent bonds between the TOCNs and silicate nanoplatelets were suggested in Fourier transform infrared (FT-IR) spectra of the composites (see Appendix). It is plausible that these interactions comprise electrostatic attractions between polar groups, such as hydroxyl groups and carboxylate groups (-COO^-Na^+) on TOCN surfaces, and aluminum oxide groups (-AlO^-Na^+) and magnesium oxide groups (-MgO^-Na^+) on MTM and SPN nanoplatelet surfaces, respectively.[14] The surfaces of both TOCNs and silicate nanoplatelets are negatively

charged in water, and they are stably dispersed even in the mixed dispersion. However, once the aqueous dispersions are dried and the composite films are formed, no nanoparticles are charged in the solid composite structures; these ionic groups on the nanoparticle surfaces are not dissociated at all in solid, which likely interact each other as polar groups. Furthermore, the dense packing of the TOCNs and silicate nanoplatelets in the composites (porosities <5%) suggests dense, strong interactions between these nanoparticles.

3.3.4 Oxygen-barrier properties

Oxygen permeabilities of the TOCN/SPN composite layers coated on PET films are shown in Figure 3.9, and detailed data are listed in Table 3.1. At 0% RH, the oxygen permeability of the composites decreased by one order of magnitude as SPN content was increased, resulting in a very low oxygen permeability value of 0.005 mL μm m^{-2} day^{-1} kPa^{-1} for the 50% w/w SPN content composite. As a reference, the oxygen permeability of ethylene vinylalcohol copolymer films, commonly used as oxygen-barrier films, are 0.01–0.1 mL μm m^{-2} day^{-1} kPa^{-1} at 0% RH.[15] However, the oxygen-barrier efficiency of the synthetic SPN nanoplatelets used in the present study is low because the aspect ratio of the SPN nanoplatelets is low (~50).[16] In the previous study, oxygen permeability of the TOCN/MTM composites at 0% RH decreased by one order of magnitude with an MTM content of only 10% w/w. At 50% RH, the oxygen permeability of the TOCN/SPN composites was high, with values of 1–2 mL μm m^{-2} day^{-1} kPa^{-1}, regardless of SPN content; no significant contribution of the SPN nanoplatelets to the oxygen permeabilities was observed. These high oxygen permeabilities at 50% RH are probably due to the 7–10% w/w moisture adsorption of the hydrophilic TOCN/SPN composites under the humid conditions.[17,18]

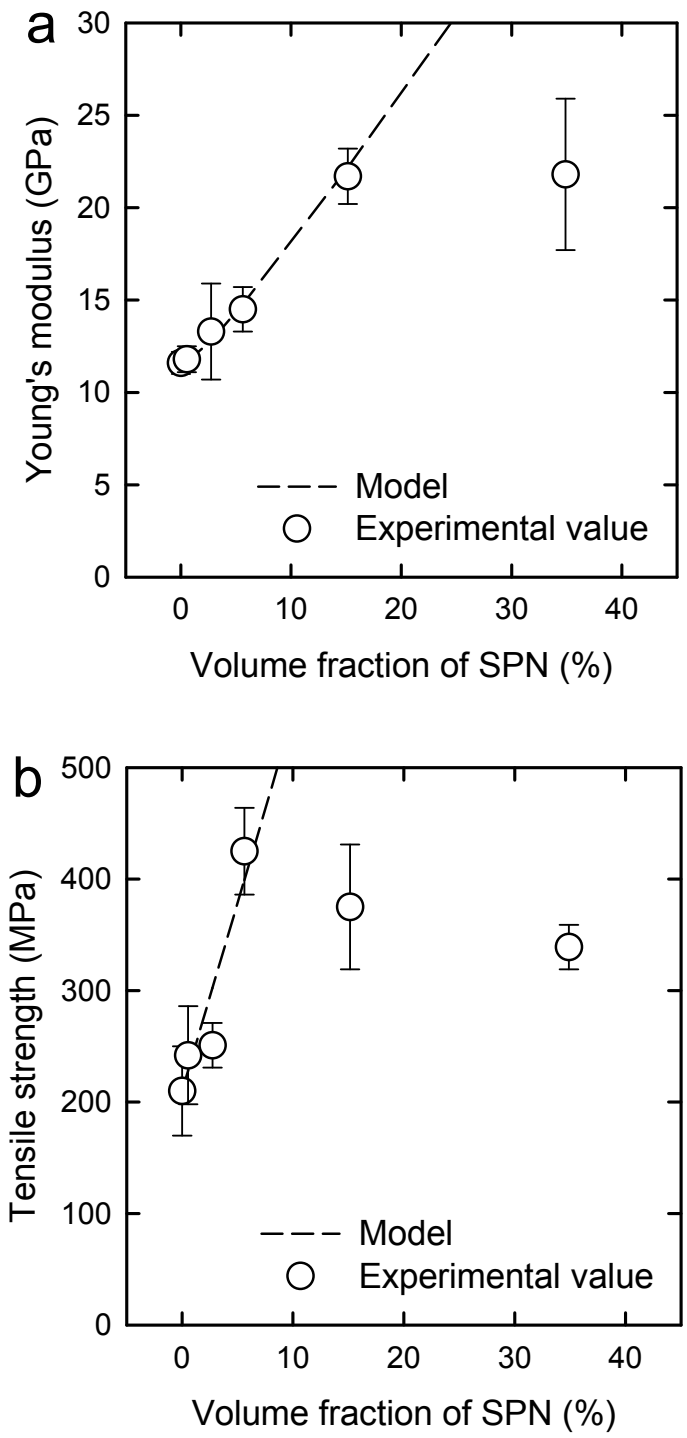

Figure 3.8. (a) Young's modulus and (b) tensile strength of the TOCN/SPN composites as a function of volume fraction of SPN nanoplatelets in comparison with models for polymer composites reinforced with low-aspect-ratio silicates. Reproduced from Journal articles No.2 in Research achievement with permission from The Royal Society of Chemistry.

Table 3.1 Mechanical and oxygen-barrier properties of the TOCN/SPN composites. Reproduced from Journal articles No.2 in Research achievement with permission from The Royal Society of Chemistry.

Sample	SPN content (% w/w)	Young's modulus (GPa)	Yield stress (MPa)	Tensile strength (MPa)	Strain-to-failure (%)	Work of fracture ($MJ\ m^{-3}$)	Oxygen permeability ($mL\ \mu m\ m^{-2}\ day^{-1}\ kPa^{-1}$)	
							0% RH	50% RH
TOCN	0	11.6 ± 0.6	143 ± 27	210 ± 40	3.2 ± 1.4	4.2 ± 2.7	0.030	1.029
TS01	1	11.8 ± 0.7	173 ± 15	242 ± 44	3.9 ± 1.5	6.3 ± 3.6	0.028	1.945
TS05	5	13.3 ± 2.6	189 ± 19	251 ± 20	4.3 ± 1.1	6.6 ± 1.8	0.018	1.585
TS10	10	14.5 ± 1.2	257 ± 18	425 ± 39	10.2 ± 1.5	29.8 ± 5.7	0.011	1.353
TS25	25	21.7 ± 1.5	270 ± 28	375 ± 56	6.5 ± 2.4	18.1 ± 7.4	0.012	1.219
TS50	50	21.8 ± 4.1	278 ± 9	339 ± 20	4.3 ± 0.7	10.7 ± 2.3	0.005	1.020

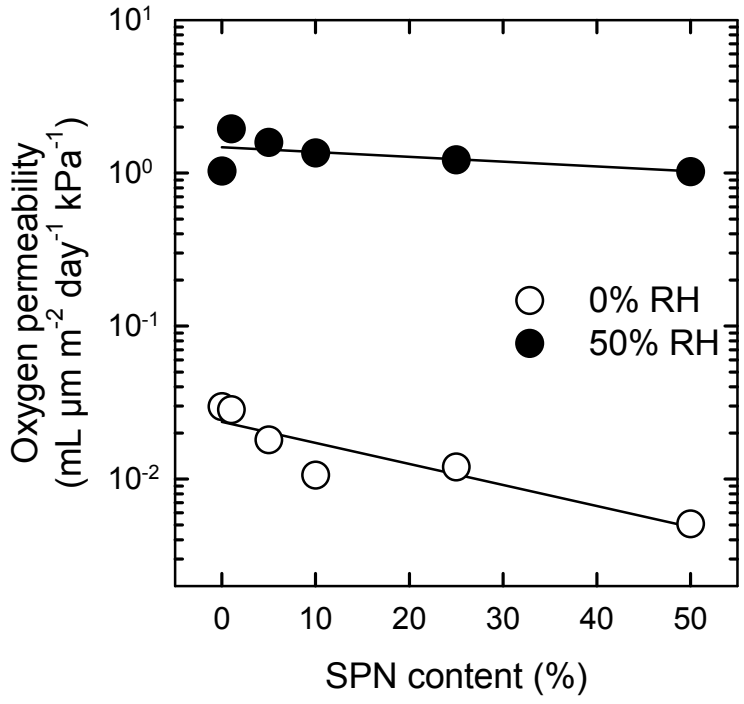

Figure 3.9. Oxygen permeabilities of the TOCN/SPN composite layers coated on PET films measured at 0% or 50% RH. Reproduced from Journal articles No.2 in Research achievement with permission from The Royal Society of Chemistry.

3.4 Conclusions

A tough and transparent PLS nanocomposite was prepared from synthetic, low-aspect-ratio SPN nanoplatelets and TOCNs. Both the SPN nanoplatelets and TOCNs have negative charges on their surfaces and are highly dispersed in water. Layered nanocomposite structures in which the SPN nanoplatelets are homogeneously distributed in the TOCN matrix are formed through a simple process of cast drying the mixed aqueous dispersions. The optical transparency of the neat TOCN matrix is maintained even as SPN nanoplatelets are incorporated at concentrations up to 50% w/w. In contrast, mechanical properties of the TOCN/SPN composites varied, depending on the SPN content. The 10% w/w SPN content composite exhibited characteristic mechanical properties of the Young's modulus of 14.5 GPa, tensile strength of 425 MPa, and strain-to-failure of 10.2%. Work of fracture of the composites increased from 4.2 to 30 MJ m^{-3} with increasing SPN content up to 10% w/w. To our knowledge, this increase of more than 7-fold in the work of fracture is unprecedented as toughening of polymer-based materials by layered silicates. These superior material properties of the TOCN/SPN composites arise from 1) the high dispersibility of both synthetic SPN nanoplatelets and TOCNs in water, 2) strong interactions between the SPN nanoplatelets and TOCNs in the solid composite, and 3) the low aspect ratio of the synthetic SPN nanoplatelets, allowing the composites to fail under the platelet-pull-out mode.

3.5 References

(1) L. J. Bonderer, A. R. Studart, and L. J. Gauckler, *Science*, **2008**, *319*, 1069–1073.

(2) B. Glavinchevski and M. Piggott, *J. Mater. Sci.*, **1973**, *8*, 1373.

(3) M. Henriksson, L. A. Berglund, P. Isaksson, T. Lindström, and T. Nishino, *Biomacromolecules*, **2008**, *9*, 1579–1585.

(4) T. Saito, T. Uematsu, S. Kimura, T. Enomae, and A. Isogai, *Soft Matter*, **2011**, *7*, 8804–8809.

(5) A. Liu, A. Walther, O. Ikkala, L. Belova, and L. A. Berglund, *Biomacromolecules*, **2011**, *12*, 633–641.

(6) T. Ebina and F. Mizukami, *Adv. Mater.*, **2007**, *19*, 2450–2453.

(7) H. Tetsuka, T. Ebina, H. Nanjo, and F. Mizukami, *J. Mater. Chem.*, **2007**, *17*, 3545–3550.

(8) H. L. Cox, *Br. J. Appl. Phys.*, **1952**, *3*, 72−79.

(9) G. E. Padawer and N. Beecher, *Polym. Eng. Sci.*, **1970**, *10*, 185−192.

(10) S. Tanpichai, F. Quero, M. Nogi, H. Yano, R. J. Young, T. Lindström, W. W. Sampson, and S. J. Eichhorn, *Biomacromolecules*, **2012**, *13*, 1340–1349.

(11) J. J Kochumalayil, M. Bergenstråhle-Wohlert, S. Utsel, L. Wågberg, Q. Zhou, and L. A Berglund, *Biomacromolecules*, **2013**, *14*, 84–91.

(12) A. Walther, I. Bjurhager, J. M. Malho, J. Pere, J. Ruokolainen, L. A. Berglund, and O. Ikkala, *Nano Lett.*, **2010**, *10*, 2742−2748.

(13) P. Podsiadlo, A. K. Kaushik, E. M. Arruda, A. M. Waas, B. S. Shim, J. Xu, H. Nandivada, B. G. Pumplin, J. Lahann, A. Ramamoorthy, and N. A. Kotov, *Science*, **2007**, *318*, 80−83.

(14) R. K. Shaha, D. L. Hunterb, and D. R. Paul, *Polymer*, **2005**, *46*, 2646–2662.

(15) J. Lange and Y. Wyser, *Packag. Technol. Sci.*, **2003**, *16*, 149−158.

(16) T. V. Duncan, *J. Colloid Interface Sci.*, **2011**, *363*, 1–24.

(17) S. S. Ray and M. Okamoto, *Prog. Polym. Sci.*, **2003**, *28*, 1539–1641.

(18) A. Isogai, T. Saito, and H. Fukuzumi, *Nanoscale*, **2011**, *3*, 71−85.

Chapter 4
Water vapor-barrier property and hydrophobicity of nanocellulose/layered silicate composites

4.1 Introduction

Water-resistant property is very important for polymeric materials. For example, packaging materials and protective films need to show stable performances under high humid conditions or even in contact with water. Cellulose is often used in packaging materials. However, cellulose-based materials are very sensitive to water, and the excellent performances of cellulose-based materials dramatically decrease under high humid conditions.

Water vapor permeability (WVP) and water contact angle (CA) are important indices to evaluate relationships between polymeric materials and water. The mechanism of WVP for polymeric materials is similar to that of oxygen gas permeability.[1] Thus, the PLS nanocomposites with high oxygen-barrier properties tend to show high water vapor-barrier property. In these high gas-barrier PLS nanocomposites, silicate nanoplatelets are in-plane oriented in the polymer matrices, resulting in the formation of the multi-walled structure that can hinder permeation of gas molecules into the materials. Therefore, the TOCN/layered silicate composites with high oxygen-barrier properties (see Chapters 2 and 3) are also expected to show high water vapor-barrier property.

CA values of solid materials are measured for evaluating hydrophobicity of the solid surfaces. When a solid surface is wetted with water droplets, these droplets compete with the surrounding air to occupy lager contact areas with the solid surface.[2] Then, the whole system reaches to an equilibrium state, and a CA between solid-liquid and liquid-gas interfaces is observed. High CA indicates that the solid surface has low surface energy, or high hydrophobicity. CA is determined by chemical composition and topology of the solid surface.[3] On the basis of this concept, a common way for increasing CA is modification of the solid surfaces with hydrophobic compounds, such as alkyl ketene dimer (AKD) that is a typical hydrophobizing chemical in papermaking industry.[4,5] Another way for increasing CA is to increase the surface roughness of materials; rough surfaces contain “air” of CA 180°

within the microstructures of the surfaces, and these air fractions can play a role for propping up the fluid from the surface. In fact, hydrophobicity of material surfaces can be improved by controlling the surface morphology, even though chemical compositions of the surfaces are hydrophilic. It has been reported that CA of lauric acid films increase from 75° to 178° by fabricating nanoscale pins perpendicular to the film surface.[6] These nanopins are covered with lauric acid and are chemically hydrophilic. However, these patterned surfaces with nanoscale pins contains an extremely high air fraction of ~99%, resulting in the induction of very high hydrophobicity.

In this Chapter, WVP and CA of the TOCN/layered silicate composites are shown. The CA values of the composites are interpreted in relation to the air fraction within the nanostructured surfaces of the composites. The air fraction is estimated based on bearing analysis by atomic force microscopy (AFM).

4.2 Experimental section

4.2.1 Materials

A softwood bleached kraft pulp, montmorillonite (MTM) powder, saponite (SPN) powder, and other chemicals were used as received. For the details, see Chapter 2.2.1 and 3.2.1.

4.2.2 Preparation of TOCN/layered silicate composite films

TOCN/layered silicate (MTM or SPN) composites were prepared according to the method described in Chapter 2. The water dispersions of TOCNs and silicate nanoplatelets were mixed by various weight ratios (99:1, 95:5, 90:10, 75:25, and 50:50) and agitated for 1h. The TOCN/layered silicate composite films were prepared by cast-drying of the mixed dispersions. The TOCN/MTM composite films with weight ratios TOCN:MTM of 99:1, 95:5, 90:10, 75:25, and 50:50 are coded as TM01, TM05, TM10, TM25, and TM50, respectively. The TOCN/SPN composite films are also coded as TS01, TS05, TS10, TS25, and TS50, respectively.

4.2.3 Characterizations

WVP of the films were determined at 37.8 ˚C using a Mocon Permatran-W Model 1/50 G (Modern Controls Inc., US). CA of 2 μL water droplets on the films were measured at 23 °C and 50% RH using a FAMAS DM500 apparatus (Kyowa Interface Science Co. Ltd., Japan). Individual silicate nanoplatelets and the film surfaces were observed by atomic force microscopy (AFM) using a Nanoscope IIIa (Veeco Instruments Inc.) equipped with a silicon nitride cantilever tip in tapping mode in air. AFM height and phase images were taken at the areas of 1 × 1 and 14 × 14 μm^2. Root-mean-square roughness (R_q) and power spectra densities of the film surfaces were calculated from the height images. On the observation of individual silicate nanoplatelets, a 0.001% w/v (5 μL) silicate nanoplatelet dispersion was dropped on a fresh cleaved surface of mica with a size of 1 × 1 cm^2 and was vacuum-dried at 60 °C for 48h. Thickness and lateral size of the nanoplatelet were measured for 135 nanoplatelets. Air area fractions at the interface between a water drop and the film surface were calculated based on the bearing analysis function in the AFM software.[7,8]

4.3 Results and discussion

4.3.1 Morphology of silicate nanoplatelets

Figure 4.1 shows AFM images of the silicate nanoplatelets used in the present study. Both the average thicknesses of MTM and SPN nanoplatelets, which were calculated from the height images, were approximately 1.1 nm. The MTM nanoplatelets are irregular in shape and have sharp edges. In contrast, SPN nanoplatelets are somewhat circular, and are very small and homogeneous in size.

Aspect ratios of MTM and SPN nanoplatelets were 281 ± 97 and 47 ± 7, respectively (Figure 4.2). On the calculation of the aspect ratios of MTM nanoplatelet, the shapes of MTM nanoplatelets with sharp edges were converted to circles with the same areas as each nanoplatelet, and the diameters of the circles were used as the length of nanoplatelet. These aspect ratios of MTM and SPN nanoplatelets are in very good agreement with the values declared by the manufacture.

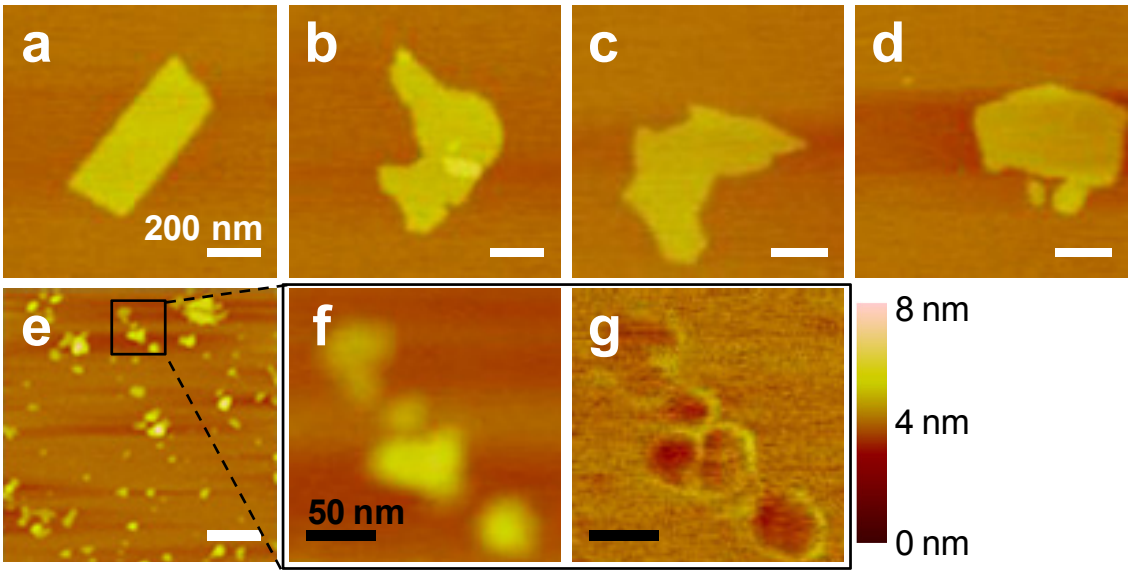

Figure 4.1. AFM height images of MTM (a, b, c, d) and SPN (e,f) nanoplatelets. The image f is a high magnification image of SPN nanoplatelets, corresponding to the black square part in the image e. (g) The phase image of the f.

4.3.2 Water vapor-barrier property

Figure 4.3 shows water vapor permeabilities (WVP) of the TOCN/layered silicate composite films. WVP of the TOCN/MTM composites decreased with increasing MTM content, and increased with increase in relative humidity (Figure 4.3a). Still under high humid conditions, the TOCN/MTM composites with high MTM contents showed significant contribution of MTM nanoplatelets to decreasing the WVP. However, the WVP of these composites were higher than those of commercial PET films that are used as water vapor-barrier materials. SPN nanoplatelets showed no significant contribution to decreasing WVP of the composites even with increasing SPN content up to 50% w/w.

Barrier mechanism for water vapor permeation into PLS nanocomposites is similar to that for oxygen gas permeation; in-plane oriented silicate nanoplatelets embedded in the polymer matrix make the diffusion path of gas molecules longer than that in neat polymer matrix.[1] Therefore, efficiency of water vapor barrier by silicate nanoplatelets with low aspect

ratios such as SPN is lower than that by high-aspect-ratio nanoplatelets with large surface areas such as MTM. The increase in WVP of TOCN/layered silicate composites under high humid conditions is explained by the hydrophilic nature of TOCNs and silicate nanoplatelets; these hydrophilic particles adsorb more moisture under high humid conditions, resulting in the expansion of the diffusion path.

4.3.3 Water contact angle

Figure 4.4 shows CA of the neat TOCN, TOCN/layered silicate composite, and neat layered silicate films. CA of the composites increased with increasing silicate content. CA of the TOCN/MTM composites increased up to ~70°, while those of the TOCN/SPN composites increased up to ~80°. These results show that hydrophilic nature of the TOCN film surfaces can be hydrophobized by distributing silicate nanoplatelets on the surfaces. However, all the elements in the composites, or TOCNs and silicate nanoplatelets, are covered with ionic groups and have no distinct hydrophobic surfaces. Thus, the increase in CA of the composites should be explained by other factor, or surface roughness.

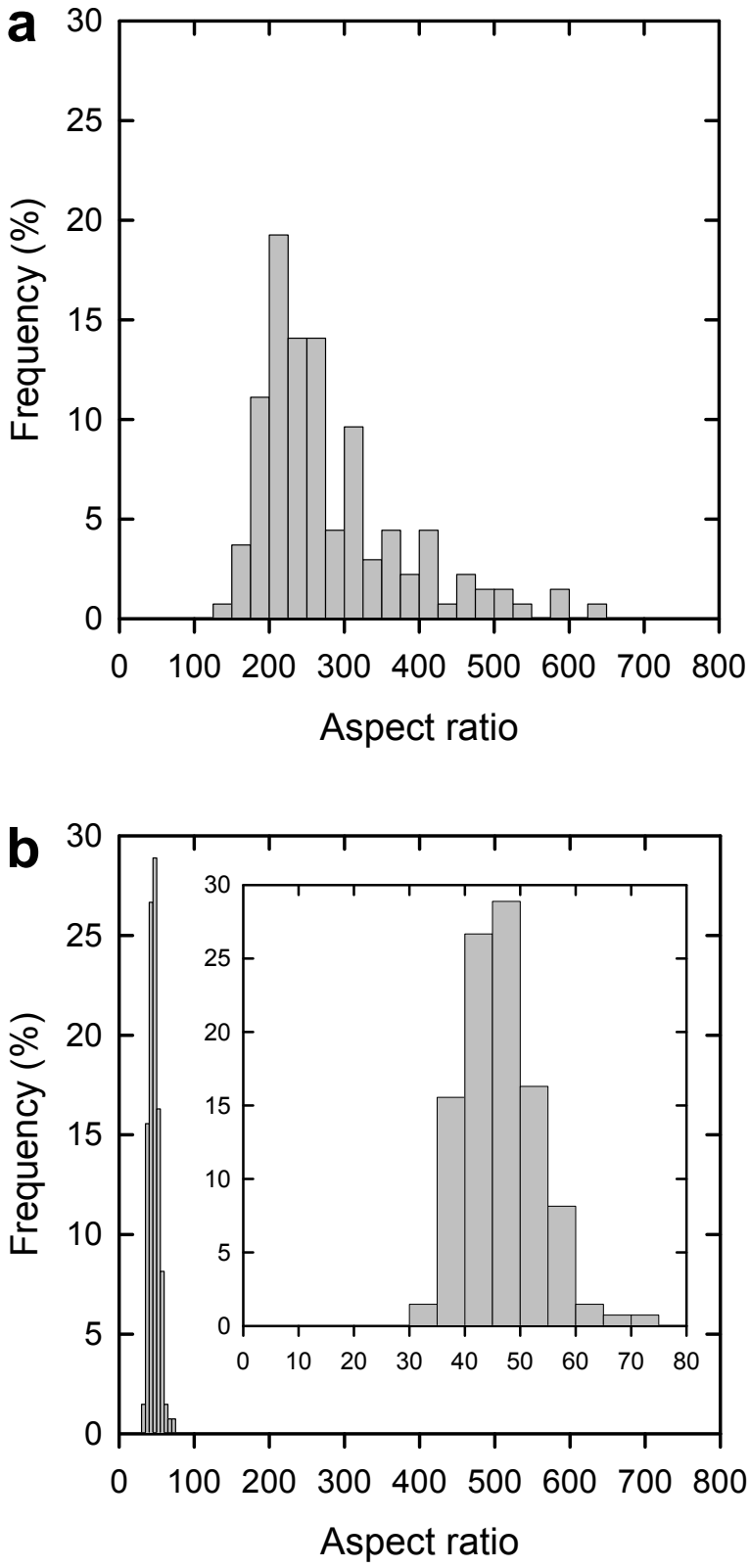

Figure 4.2. Aspect ratio distributions of (a) MTM and (b) SPN nanoplatelets.

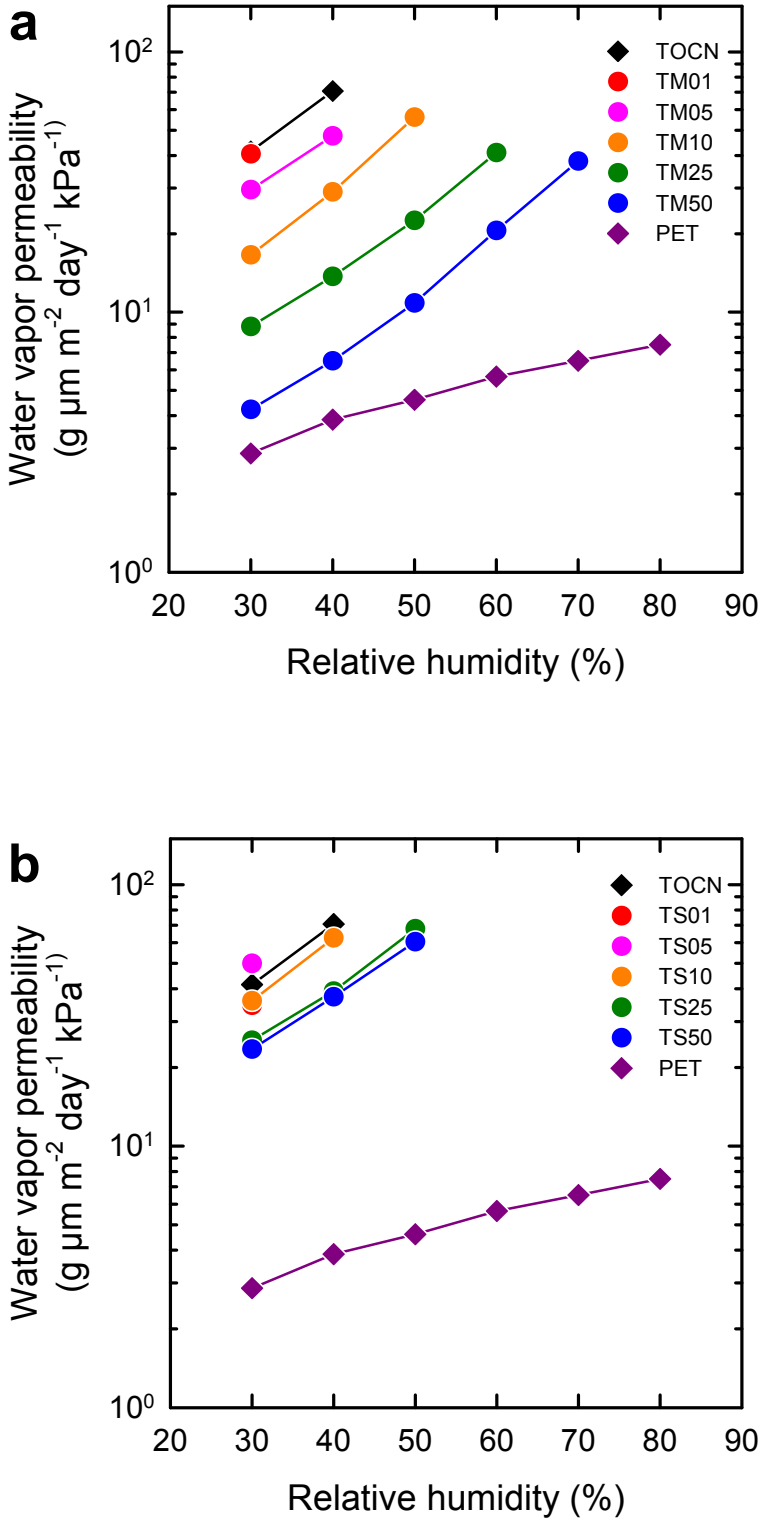

Figure 4.3. WVP of the (a) TOCN/MTM and (b) TOCN/SPN composite films at different relative humidities. WVP of a commercial PET film is shown as a reference.

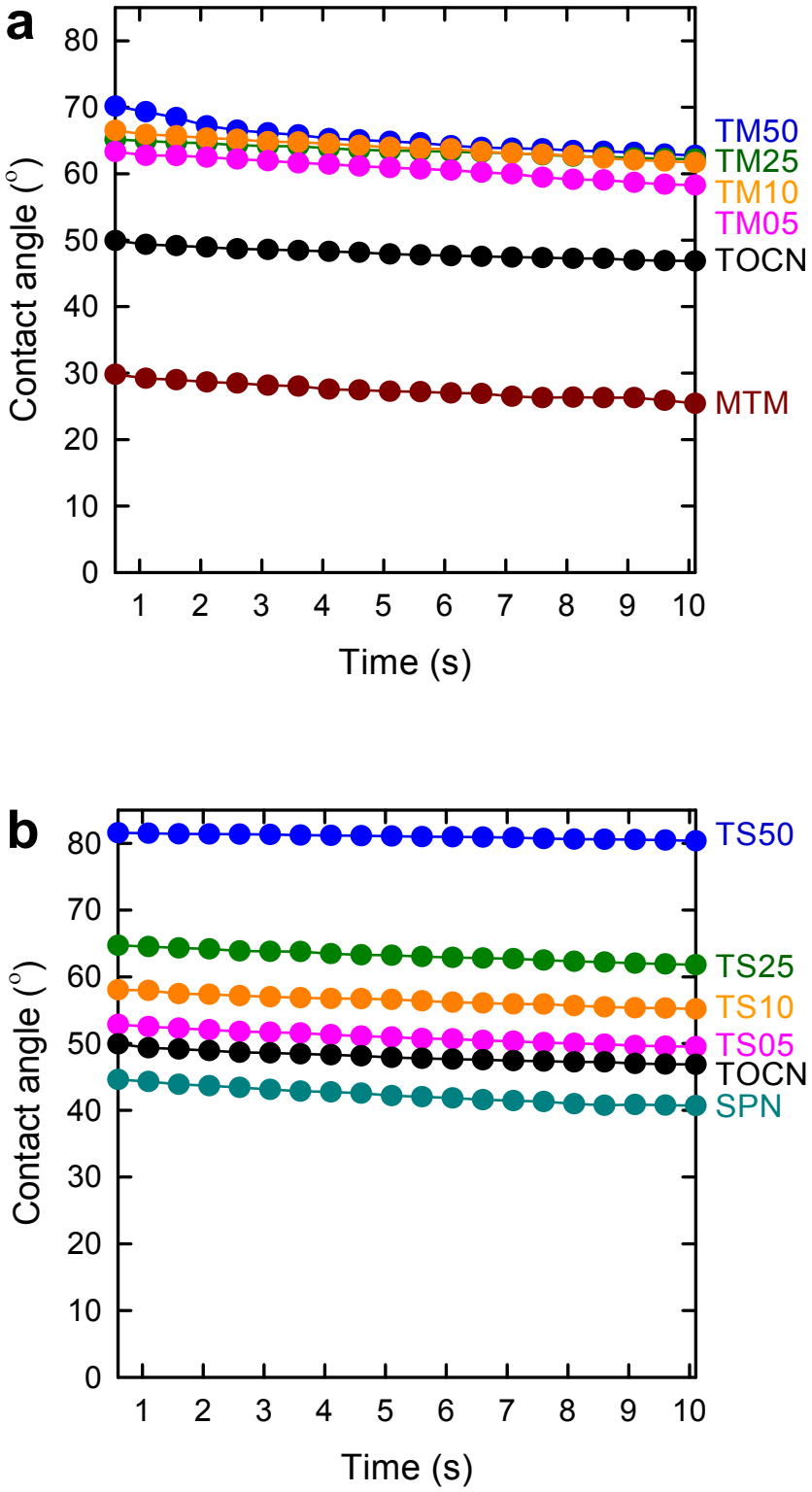

Figure 4.4. (a) CA of the neat TOCN, TOCN/MTM composite, and neat MTM films. (b) CA of the neat TOCN, TOCN/SPN composite, and neat SPN films.

4.3.4 Surface roughness

Figure 4.5 shows AFM images of the surfaces of the TOCN, TM50, and TS50 films. For the neat TOCN film, nanofibrillar structures were clearly observed in both the height and phase images (Figures 4.5a and 4.5b). In contrast, for the TM50 and TS50 composite films, grain boundaries of TOCNs and silicate nanoplatelets were obscure in the height images (Figures 4.5c and 4.5e), while they are clearly identified in the phase images (Figures 4.5d and 4.5f). The phase image is a helpful tool to identify the surface elements that are difficult to be observed by height image; the phase image is topological data based on adhesion forces between the tip and material surface and is independent from the fluctuation of height profiles.[9] The sizes of MTM and SPN nanoplatelets on the film surfaces observed in the phase images well correspond to the lateral sizes of individual silicate nanoplatelets dispersed on flat mica surfaces (Figures 4.1 and 4.2), suggesting that silicate nanoplatelets are in-plane oriented not only within the composites but also on the film surfaces.

Root-mean-square roughness (R_q) and spatial wavelengths were calculated from the AFM height profiles for the surface areas of 14 × 14 μm^2 (Figure 4.6 and Table 4.1). The TOCN/layered silicate composites had higher R_q values and longer spatial wavelengths than the neat TOCN film. And, the MTM composites had much higher R_q values and longer spatial wavelengths than the SPN composites. The R_q is a parameter to quantify the surface roughness of materials.[10,11] A high R_q value means sharp change of height in the vertical direction. However, it is not objective to describe surface topology of materials only by R_q. The R_q is unable to reflect the height change in the horizontal direction, such as distance between two adjacent hills. Instead, the spatial wavelength, which is calculated from power spectra density of the height image, shows the height change in the horizontal direction.[10,11]

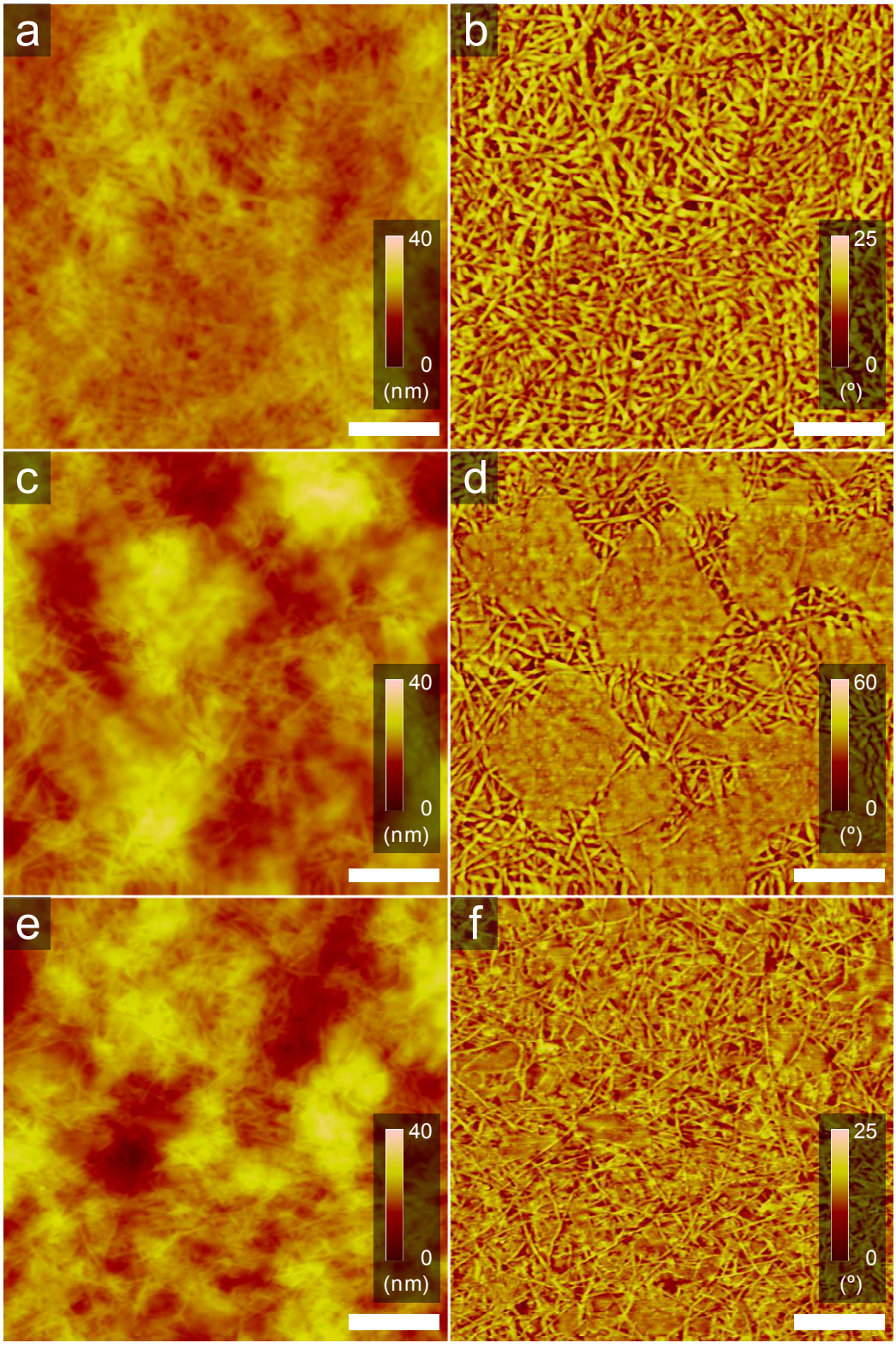

Figure 4.5. AFM height images (a, c, e) and phase images (b, d, f) of the surfaces of the TOCN, TM50, and TS50 films. The scale bars are 200 nm.

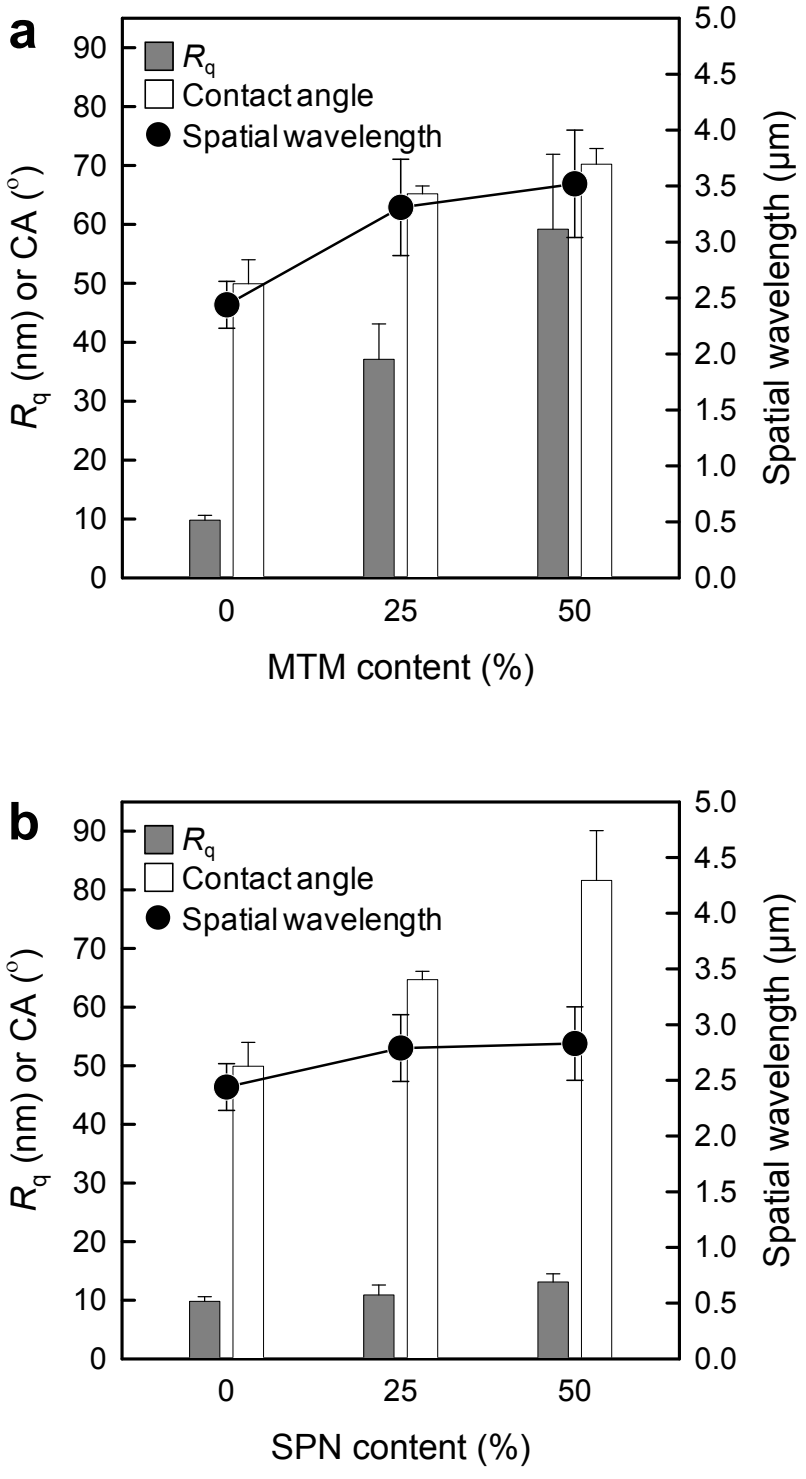

Figure 4.6. R_q, CA, and spatial wavelengths of the (a) TOCN/MTM and (b) TOCN/SPN composite films. The R_q values and spatial wavelengths were calculated from the AFM height profiles for the surface areas of 14 x 14 μm^2.

Table 4.1. CA, R_q, spatial wavelengths, and air area fractions of the TOCN/layered silicate composites.

Sample	CA (°)	R_q (nm)	Spatial wavelength (μm)	Air area fraction (%)
TOCN	49.9 ± 4.1	9.8 ± 0.8	2.44 ± 0.21	18.2 ± 2.6
TM25	65.2 ± 1.3	37.1 ± 6.0	3.31 ± 0.43	30.9 ± 10.1
TM50	70.2 ± 2.7	59.2 ± 12.7	3.52 ± 0.48	33.0 ± 7.9
TS25	64.7 ± 1.4	10.9 ± 1.7	2.79 ± 0.30	27.7 ± 4.7
TS50	81.6 ± 8.5	13.1 ± 1.4	2.83 ± 0.33	38.4 ± 5.2

4.3.5 Relationship between contact angle and surface roughness

As shown in Figure 4.6, the CA are correlated to the R_q values and spatial wavelengths of the composites; the CA increased with increase in R_q value or spatial wavelength. However, the increase in CA was unexplained solely by either R_q value or spatial wavelength (Figure 4.7). The correlation coefficients, or r^2 values, between the CA and either R_q value or spatial wavelength were low. Thus, air fractions within microstructures of the film surfaces should be taken into consideration to explain this unusual phenomenon.[6] The following equation, known as Cassie's law, is often used to explain CA of solid material surfaces,

$$\cos\theta_c = f_1 \cos\theta_1 + f_2 \cos\theta_2 \tag{4.1}$$

where θ_c is contact angle of the solid surface, and θ_1 and θ_2 are contact angles of the ideally flat surfaces of element 1 and 2, respectively, and f_1 and f_2 are area fractions of element 1 and 2 on the solid surface, respectively, and $f_1 + f_2 = 1$.[12] When the element 2 is air, or the solid surface is uneven, equation 4.1 is simplified by substituting CA 180° of air to θ_2 as follows,

$$\cos\theta_c = \cos\theta_1 - f_{air}(\cos\theta_1 + 1) \tag{4.2}$$

where f_{air} is the area fraction of air on the solid surface. Furthermore, when the solid element

is ideally hydrophilic, $\theta_l = 0$, resulting in the following equation,

$$\cos\theta_c = 1 - 2f_{air} \tag{4.3}$$

In the present study, all the elements in the composites, or TOCNs and silicate nanoplatelets, are covered with ionic groups and have no hydrophobic surfaces. Thus, it is reasonable that theoretical CA values of the film surfaces are calculated using equation 4.3.

The area fractions of air on the film surfaces were calculated from the AFM height profiles by the bearing analysis (Table 4.1).[7,8] The height from the lowest position of the microstructured surface is defined as a bearing height. The air area fraction on the microstructured surface is a function of the bearing height and increases with increase in bearing height. The real height of the air fraction under a water droplet on the microstructured surface is unmeasurable. Hence, height values z_i obtained by subtracting the height profiles of the microstructured surface from a bearing height are assumed to be the heights of the air fraction under a water droplet. Here, the bearing height is assumed to be an average height of the water droplet from the lowest position of the microstructured surface. In fact, when the height value z_i at a position is positive, the position is recognized as the air fraction under a water droplet in the bearing analysis.

Figure 4.8 shows relationship between the CA and the air area fractions that were calculated based on the bearing analysis assuming that the bearing height is $0.3R_{max}$. The R_{max} value is the difference in height between the highest and the lowest positions of the microstructured surface. The dashed line in this figure shows a theoretical relationship described by equation 4.3. The best fitting of the air area fractions of the composites to the theoretical line was observed when the bearing height was $0.3R_{max}$. This result indicates that the average height of a water droplet from the lowest position of the film surface was about $0.3R_{max}$. The CA values had a very good correlation with the air area fractions when compared to the correlation with R_q value or special wavelength (see Figure 4.7), and the CA values almost linearly increased with increase in the air area fraction.

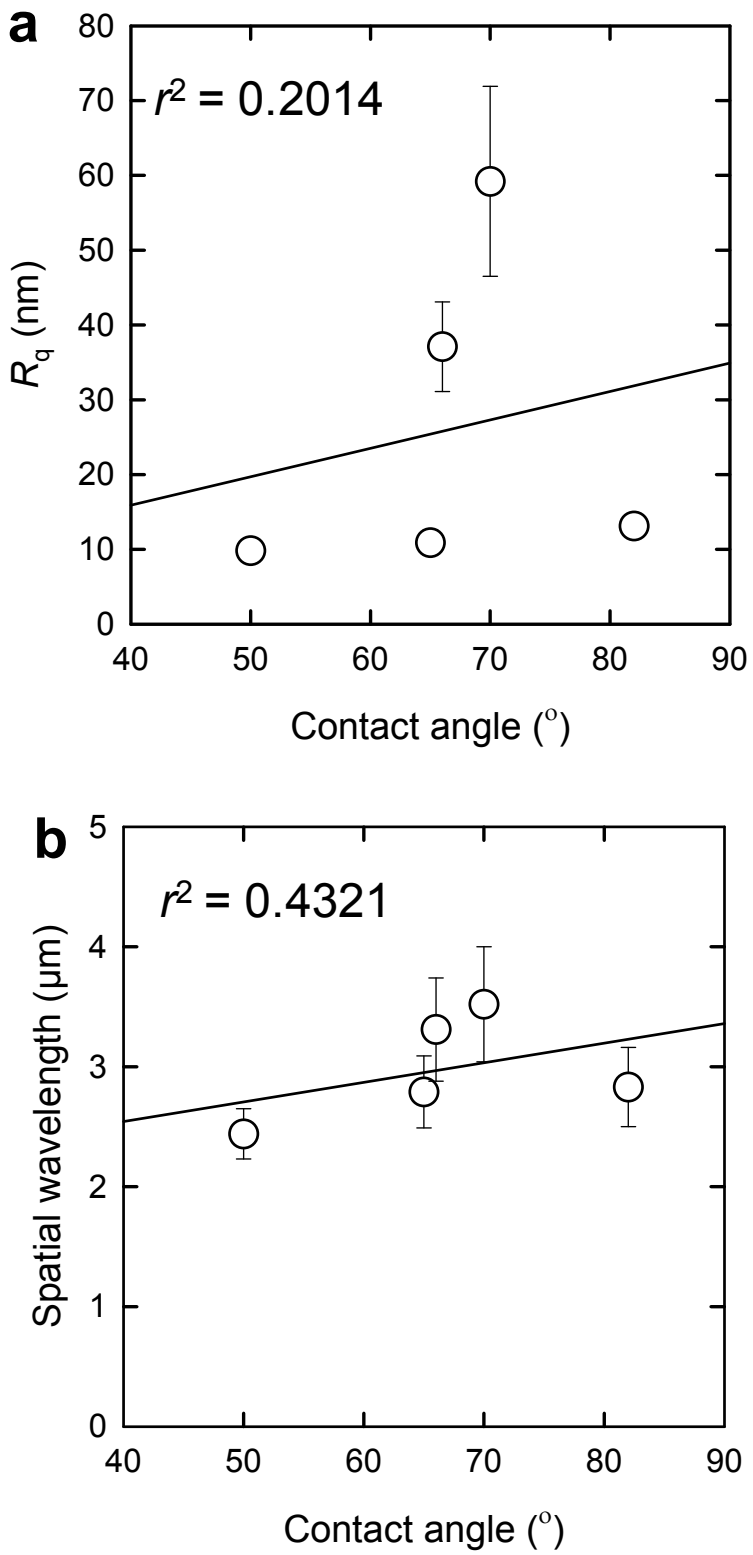

Figure 4.7. Relationships between the CA and either (a) R_q value or (b) spatial wavelength of the TOCN/layered silicate composite and neat TOCN film surfaces.

It is interesting that the TS50 film showed a lower R_q value and a shorter spatial wavelength yet a larger air area fraction than the TM50 film. This phenomenon is probably related to the sizes of silicate nanoplatelets on the composite surfaces. Figure 4.9 shows three-dimensional AFM height images of the TM50 and TS50 film surfaces. The MTM nanoplatelets of high aspect ratio form a wide and large hill on the TM50 film surface. In contrast, the SPN nanoplatelets of low aspect ratio form a narrow and small hill on the TS50 film surface, which is likely to give a lower R_q value, a shorter spatial wavelength, and a larger air area fraction than the microstructure of TM50 film surface.

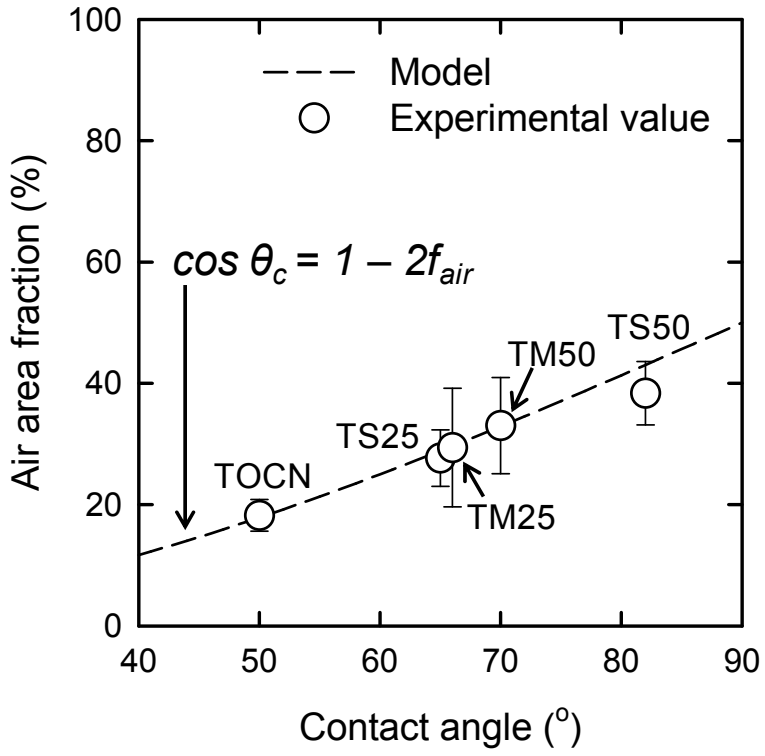

Figure 4.8. Relationship between the CA and the air area fractions on the surfaces of the TOCN/layered silicate composite and neat TOCN films. The dashed line shows a theoretical relationship described by equation 4.3.

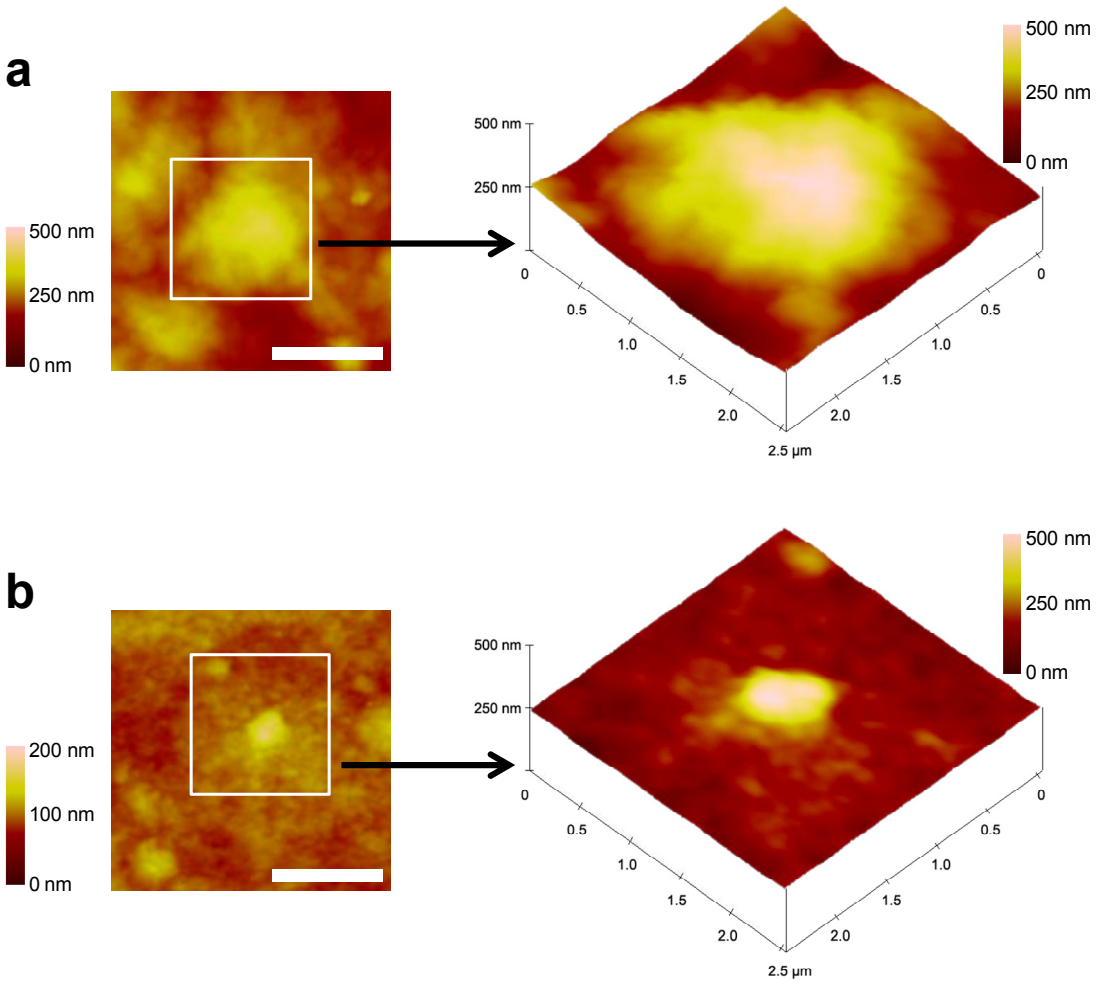

Figure 4.9. Three-dimensional AFM height images of the (a) TM50 and (b) TS50 film surfaces. The scale bars are 2 μm.

4.4 Conclusions

WVP and CA of the TOCN/layered silicate composite films were investigated. WVP of the TOCN/MTM composites decreased with increasing MTM content and showed significantly low WVP even under high humid conditions. In contrast, SPN nanoplatelets of low aspect ratio showed no significant contribution to decreasing WVP of the composites even with increasing SPN content up to 50% w/w. These results are explained by the difference in aspect ratio of silicate nanoplatelets; silicate nanoplatelets with high aspect ratios make the diffusion path of gas molecules within the polymer matrix longer than those with low aspect ratios. CA

of the TOCN/layered silicate composite films increased with increasing layered silicate content, whereas CA of the neat TOCN and neat layered silicate films were very low. Both the TOCNs and silicate nanoplatelets are covered with ionic groups and have no distinct hydrophobic surfaces. Therefore, the increase in CA was explained by increase in the air area fraction within the microstructured surface of the composite. The air area fractions were calculated from the AFM height profiles of the film surfaces by bearing analysis. As a result, the CA values had a very good correlation with the air area fractions when compared to the correlation with R_q value or spatial wavelength, and the CA values almost linearly increased with increase in the air area fraction. It is interesting that assembly of hydrophilic nanoparticles with different shapes, or the composite films of nanofibrils and nanoplatelets, gave higher CA than that of uniformly-shaped nanoparticles, or neat nanofibril and neat nanoplatelet films.

4.5 References

(1) T. V. Duncan, *J. Colloid Interface Sci.*, **2011**, *363*, 1−24.

(2) A. Marmur, *Soft Matter*, **2013**, *9*, 7900−7904.

(3) L. Feng, S. Li, Y. Li, H. Li, L. Zhang, J. Zhai, Y. Song, B. Liu, L. Jiang, and D. Zhu, *Adv. Mater.*, **2002**, *14*, 1857–1860.

(4) H. Fukuzumi, T. Saito, T. Iwata, Y. Kumamoto, and A. Isogai, *Biomacromolecules*, **2009**, *10*, 162−165.

(5) Q. Yang, T. Saito, and A. Isogai, *Cellulose*, **2012**, *19*, 1913–1921.

(6) E. Hosono, S. Fujihara, I. Honma, and H. Zhou, *J. Am. Chem. Soc.*, **2005**, *127*, 13458−13459.

(7) A. Mardilovich and E. Kokkoli, *Langmuir*, **2005**, *21*, 7468–7475.

(8) M. Harris, G. Appel, and H. Ade, *Macromolecules*, **2003**, *36*, 3307–3314.

(9) I. Schmitz, M. Schreiner, G. Friedbacher, and M. Grasserbauer, *Appl. Surf. Sci.*, **1997**, *115*, 190−198.

(10) R. Gavrila, A. Dinescu, and D. Mardare, *Rom. J. Inf. Sci. Tech.*, **2007**, *10*, 291–300.

(11) A. Duparré, J. F.-Borrull, S. Gliech, G. Notni, J. Steinert, and J. M. Bennett, *Appl. Opt.*, **2002**, *41*, 154–171.

(12) A. B. D. Cassie and S. Baxter, *Trans. Faraday Soc.*, **1944**, *40*, 546–561.

Chapter 5
Summary

A new type of biobased PLS nanocomposites has been developed from nanofibrillar cellulose and layered silicate through a simple process of cast-drying their aqueous dispersions. Both cellulose and silicate are abundant in nature. The nanofibrillar cellulose used in the present study are chemically modified by topological surface oxidation using TEMPO as a catalyst. The resulting TEMPO-oxidized cellulose nanofibril (TOCN)/layered silicate composites have closely-packed layered nanostructures, in which the silicate nanoplatelets are homogeneously distributed in the TOCN matrices. These composites have low densities yet exhibit excellent performances in mechanical and oxygen-barrier properties. The material properties of the composites, however, strongly depend on the aspect ratios of the silicate nanoplatelets. In the preset study, natural MTM and synthetic SPN nanoplatelets were used as the layered silicates. MTM nanoplatelets have higher aspect ratios than SPN ones, while SPN nanoplatelets have higher dispersibility in water than MTM ones. These characteristics of MTM and SPN nanoplatelets govern the material properties of the TOCN/layered silicate composites as follows,

Optical transparency (Figure 5.1): The neat TOCN films are optically transparent. However, light transmittance of the TOCN/MTM composites linearly decreases with increasing MTM content. In contrast, the TOCN/SPN composites are transparent regardless of SPN content, which can be explained by the higher dispersibility of SPN nanoplatelets in the TOCN matrices.

Mechanical property (Figure 5.2): Mechanical properties of the TOCN/MTM composites are characterized by extremely high tensile strength of over 500 MPa, while those of the TOCN/SPN composites are characterized by high toughness of up to 30 MJ m^{-3}. These characteristics in mechanical properties can be interpreted based on models for fracture behavior of PLS composites; high-aspect-ratio MTM nanoplatelets of high surface area can accept sufficient interfacial shear stress to be fractured in the composite, giving the composites with high ultimate strength, while low-aspect-ratio SPN nanoplatelets of low surface area are pulled out from the polymer matrix, giving the composites with high strain-to-failure or high toughness. These excellent mechanical properties of the

TOCN/layered silicate composites should arise from strong interactions at the interfaces between the TOCNs and silicate nanoplatelets in the composite. It is plausible that these interactions comprise electrostatic attractions between polar groups, such as hydroxyl groups and carboxylate groups (-COO^-Na^+) on TOCN surfaces, and aluminium oxide groups (-AlO^-Na^+) and magnesium oxide groups (-MgO^-Na^+) on silicate nanoplatelet surfaces. The surfaces of both TOCNs and silicate nanoplatelets are negatively charged in water, and they are stably dispersed even in the mixed dispersion. However, once the aqueous dispersions are dried and the composite films are formed, no nanoparticles are charged in the solid composite structures; these ionic groups on the nanoparticle surfaces are not dissociated in solid, which likely interact each other as polar groups.

Gas-barrier property (Figure 5.3): Oxygen- and water vapor-barrier properties of the TOCN/MTM composites are much higher than those of the TOCN/SPN composites. This is because the surface areas of high-aspect-ratio MTM nanoplatelets are much larger than those of low-aspect-ratio SPN ones, which makes the diffusion path of gas molecules longer. The oxygen- and water vapor-barrier properties of the TOCN/MTM composites are significantly improved with increasing MTM content. In contrast, SPN nanoplatelets showed no significant contribution to the improvement of gas-barrier properties of the composites.

Hydrophobicity: Water contact angles (CA) of both the TOCN/MTM and TOCN/SPN composites increase with increasing silicate content. However, all the nanoparticles in the composites, or TOCNs, MTM and SPN nanoplatelets, are hydrophilic and have no hydrophobic surfaces. The increase in CA is thus explained by increase in the air area fraction on the microstructured surfaces of the composites; the air area fraction can be calculated from the AFM height profiles of the composite surfaces using the bearing function. The air area fraction on the composite surfaces increases with increasing MTM or SPN content, and the CA values of the composites almost linearly increase with the increase in the air area fraction.

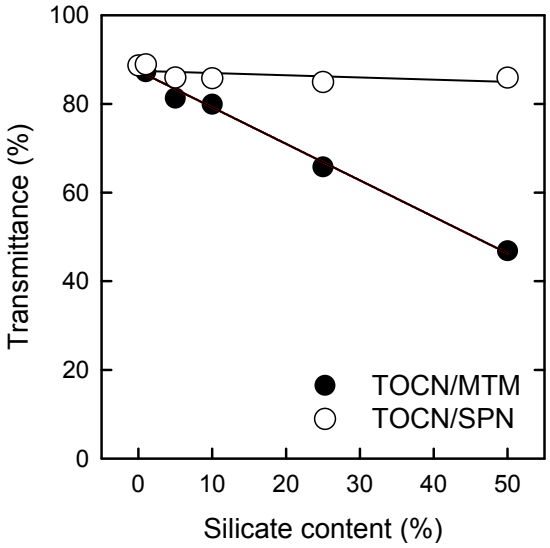

Figure 5.1. Light transmittances of the TOCN/MTM and TOCN/SPN composite films at 600 nm wavelength.

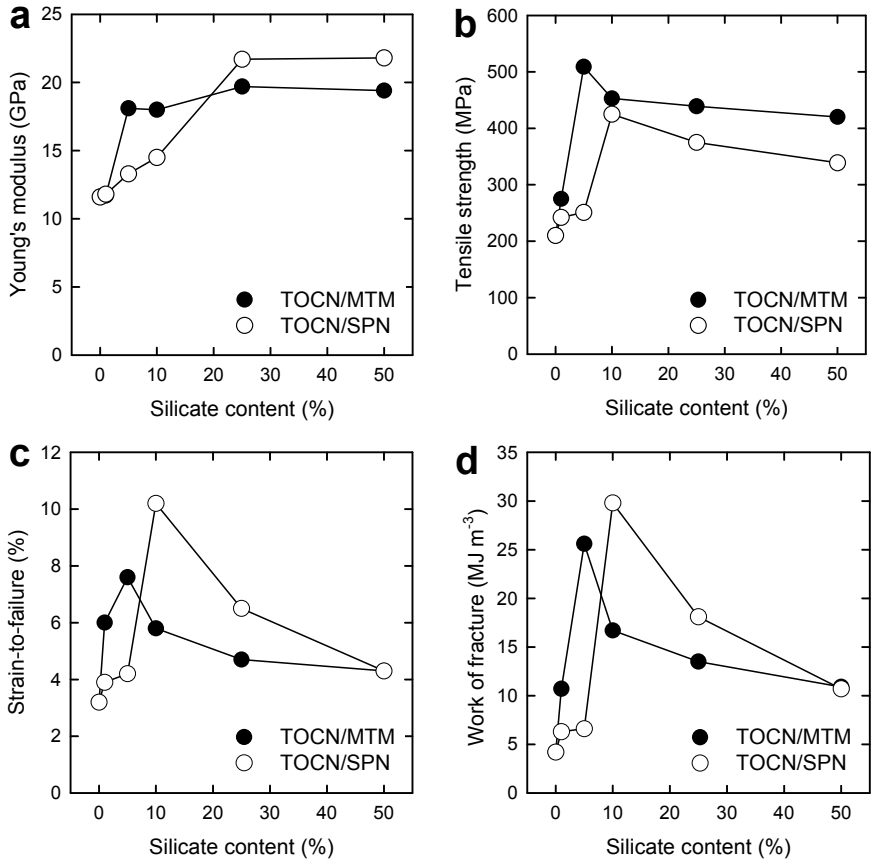

Figure 5.2. Mechanical properties of the TOCN/MTM and TOCN/SPN composite films. (a) Young's moduli. (b) Tensile strengths. (c) Strains-to-failure. (d) Works of fracture.

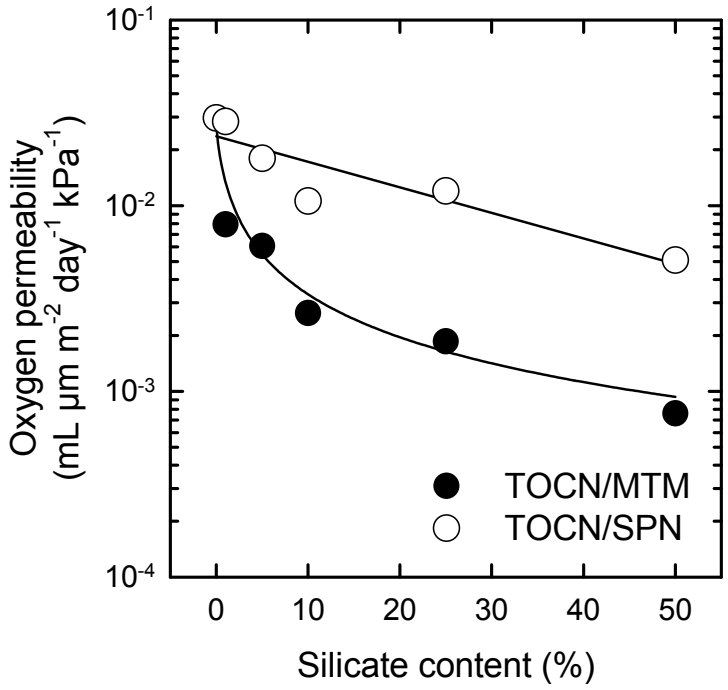

Figure 5.3. Oxygen permeabilities of the TOCN/MTM and TOCN/SPN composite films at 0% relative humidity.

Appendix

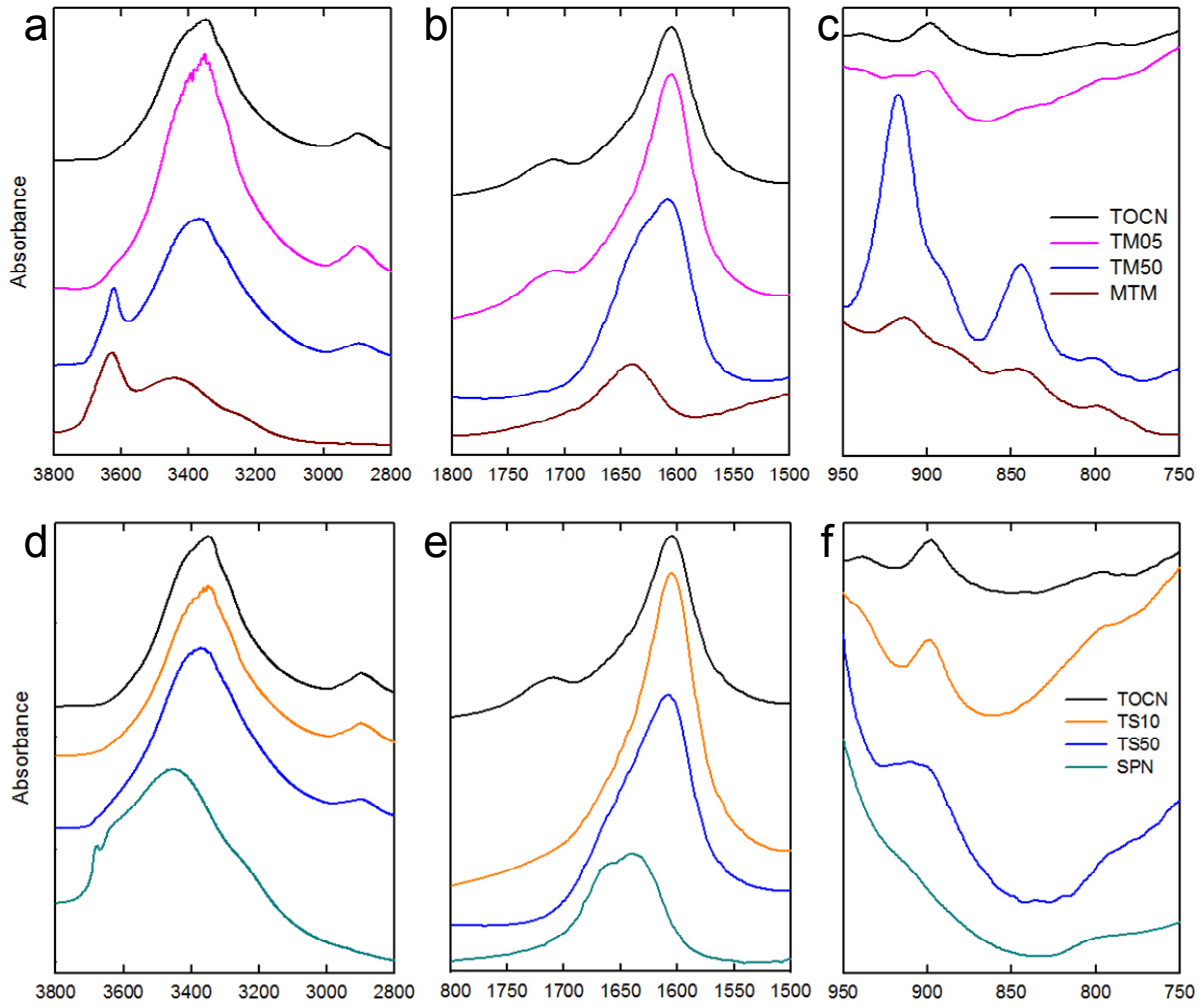

Figure A.1. The FT-IR spectra of the TOCN/MTM (a, b, c) and TOCN/SPN (d, e, f) composite films. The spectra were recorded using a JASCO FT/IR-6100 spectrometer in transmission mode with a resolution of 4 cm^{-1}. It has been reported that a vibration peak at 848 cm^{-1} is observed when Al-O-C bonds are formed in the composites.[1]

(1) P. Podsiadlo, A. K. Kaushik, E. M. Arruda, A. M. Waas, B. S. Shim, J. Xu, H. Nandivada, B. G. Pumplin, J. Lahann, A. Ramamoorthy, and N. A. Kotov, *Science*, **2007**, *318*, 80−83.

Research achievement

Journal articles

1. Chun-Nan Wu, Tsuguyuki Saito, Shuji Fujisawa, Hayaka Fukuzumi, and Akira Isogai, "Ultrastrong and High Gas-Barrier Nanocellulose/Clay-Layered Composites", *Biomacromolecules*, ACS publications, **2012**, *13*, 1927−1932.

2. Chun-Nan Wu, Quanling Yang, Miyuki Takeuchi, Tsuguyuki Saito, and Akira Isogai, "Highly tough and transparent layered composites of nanocellulose and synthetic silicate", *Nanoscale*, RSC publishing, **2014**, *6*, 392−399.

3. Chun-Nan Wu, Tsuguyuki Saito, Quanling Yang, Zi-Dong Qi, Hayaka Fukuzumi, and Akira Isogai, "Hydrophobic Nature Exhibited by the Nanostructured Surfaces of Hydrophilic Assemblies of Nanocellulose Fibrils and Nanoclay Platelets", to be submitted.

4. Quanling Yang, Chun-Nan Wu, Tsuguyuki Saito, and Akira Isogai, "Cellulose-clay layered nanocomposite films fabricated from aqueous cellulose/LiOH/urea solution", *Carbohydrate Polymers*, Elsevier, **2014**, *100*, 179−184.

Conferences

International conferences

1. Chun-Nan Wu, Tsuguyuki Saito, Shuji Fujisawa, Hayaka Fukuzumi, and Akira Isogai, "Ultrastrong and High Gas-Barrier Biocomposite Films of TEMPO-Oxidized Cellulose Nanofibrils and Clay Nanoplatelets", *The 243rd American Chemical Society (ACS) National Meeting*, San Diego, CA, USA, Mar. **2012**. [Oral]

2. Chu-Nan Wu, Tsuguyuki Saito, Shuji Fujisawa, Hayaka Fukuzumi, and Akira Isogai, "Ultrastrong and High Oxygen-barrier Bionanocomposites of Nanofibrous Cellulose and Clay Mineral", *Nanofibers 2012*, Tokyo, Japan, Jun. **2012**. [Poster]

3. Chun-Nan Wu, Quanling Yang, Miyuki Takeuchi, Tsuguyuki Saito, and Akira Isogai, "Highly tough and transparent layered composites of nanocellulose and clay nanoplatelets", *The 3rd International Cellulose Conference (ICC)*, Sapporo, Japan, Oct. **2012**. [Poster]

4. Chun-Nan Wu, Tsuguyuki Saito, Quanling Yang, Miyuki Takeuchi, Zi-Dong Qi, Hayaka Fukuzumi, and Akira Isogai, "Hydrophobic and Tough Composites of Nanocellulose and Synthetic Layered Silicate", *European Polysaccharide Network of Excellence (EPNOE) 2013 International Polysaccharide Conference*, Nice, France, Oct. **2013**. [Oral]

Conferences in Japan

1. Chun-Nan Wu, Tsuguyuki Saito, Shuji Fujisawa, Hayaka Fukuzumi, and Akira Isogai, "Preparation and property analyses of TOCN/nanoclay composites", *The 18th Annual Meeting of the Cellulose Society of Japan*, Nagano, Japan, Jul. **2011**. [Poster]

2. Chun-Nan Wu, Tsuguyuki Saito, Quanling Yang, and Akira Isogai, "Ultrastrong and Transparent TOCN/nanoclay Composites", *The 19th Annual Meeting of the Cellulose Society of Japan*, Nagoya, Japan, Jul. **2012**. [Poster]

3. Chun-Nan Wu, Quanling Yang, Miyuki Takeuchi, Zi-Dong Qi, Tsuguyuki Saito, and Akira Isogai, "Highly Tough and Transparent TOCN/nanoclay Composites", *The 63rd Annual Meeting of the Japan Wood Research Society*, Morioka, Japan, Mar. **2013**. [Oral]

Patent

Akira Isogai, Chun-Nan Wu, and Tsuguyuki Saito, Cellulose nanofibril composites and the preparative method, Japan Patent, P2013−10891A, Jan. **2013**.

Honor and award

Interchange Association, Japan (IAJ) scholarship for international students from Taiwan, Apr. 2010−Mar. 2014.

Acknowledgement

This thesis is a compilation of studies carried out from April 2011 to March 2014 under the supervision of Professor Akira Isogai in the University of Tokyo. I would like to express my deepest gratitude to Professor Isogai for his warm encouragement and considerate guidance throughout this study, as well as his support, kindness and toleration to me. I will never forget Professor Isogai's sense of humor and quizzes of Oricon chart.

Moreover, I would like to express my sincere gratitude to Associate Professor Tsuguyuki Saito. Associate Professor Saito gave me constructive instruction and taught me logical thinking, skills of scientific writing, and great fundamental knowledge about this study.

In addition, I would like to thank Professor Minoru Kimura for his encouragements, advices, and interesting conversations about life experiences and international relationship. And, I am grateful to Assistant Professor Miyuki Takeuchi for the help and advices of electronic microscopy. Furthermore, I am also grateful to Professor Toshiharu Enomae of University of Tsukuba for his kind encouragement and suggestions. Besides, appreciation was attributed to Professor Song-Yung Wang and Professor Shang-Tzen Chang of National Taiwan University, Taiwan, and Professor Naoto Ando for their supports and advices for my studying abroad.

Next, I would like to acknowledge Dr. Hayaka Fukuzumi of Tokyo Institute of Technology for her generous support for my experiments, especially knowledge about barrier properties, and daily life. I am grateful to Dr. Quanling Yang for the help of X-ray diffraction (XRD) analysis, water vapor permeability, water contact angle, and many helpful discussions on material science. Also, I am grateful to Mr. Syuji Fujisawa for the help of experiments and support for daily life. Appreciation was given to Mr. Zi-Dong Qi for the help of atomic force microscopy and sharing interesting things, Mr. Ryota Kuramae for the help of energy-dispersive X-ray (EDX) analysis, Assistant Professor Hirotaka Koga of Osaka University for experimental advices and encouragement, Ms. Yuko Ono for the help of all the documents and warm concern, Associate Professor Ramaiah Neelam and Ms. Tae Ito of OICE for the support to an international student. In addition, I would like to acknowledge all the lab members for the support for this study and daily life, advices of Japanese, sharing life

experiences, and conversations about Japanese pop and rock songs, which are my favorites forever.

Special thanks to Professor Akira Isogai, Professor Tadahisa Iwata, Associate Professor Akio Takemura, Associate Professor Masahisa Wada, and Associate Professor Tsuguyuki Saito for their remarkable contributions to the revision of this thesis.

I sincerely thank my warm family in Taiwan for their encouragement. I am also thankful to all the Taiwanese international students who worked hard with me.

Particularly, considerable acknowledgement was given to Interchange Association, Japan (IAJ) for the financial support. Without their scholarship, I could not study abroad to Japan and finish this study.

Finally, I would like to express my gratitude again to all the people who helped and supported me in these years. This wonderful journey will be unforgettable in my life.